nature communications

Article

https://doi.org/10.1038/s41467-026-70978-z

PD-1 blockade plus tyrosine kinase inhibitor remodels the tumor microenvironment in advanced renal cell carcinoma

Received: 6 August 2025

Accepted: 9 March 2026

Published online: 31 March 2026

Check for updates

Liangyou Gu[1,6], Qi Zhang[2,6], Qiyang Liang[1,3,6], Cheng Peng[1,6], Yaohui Wang[1,6], Chenfeng Wang[4], Zhuoran Li[1,5], Yezhen Tan[2], Yanming Zhou[1,3], Qing Bi[1,3], Xiubin Li[1], Jin Luo[1,5], Qingbo Huang[1], Yan Huang[1] ✉, Xu Zhang[1] ✉, Xin Ma[1] ✉, Weimin Ci[1] ✉ & Baojun Wang[1] ✉

The combination of tyrosine kinase inhibitors (TKIs) and immune checkpoint inhibitors (ICIs) has improved clinical outcomes in advanced renal cell carcinoma (aRCC), though therapeutic resistance remains a major challenge. We conducted single-cell transcriptomic analysis on 61 tumor samples from 34 aRCC patients treated with TKIs alone or in combination with ICIs. Non-responders exhibited increased neutrophil infiltration and enrichment of SAA^+ tumor cells following treatment. We identified a $VEGFA^+CEACAM1^+$ neutrophil subset exhibiting immunosuppressive properties that is associated with poor clinical response. In vivo, pharmacologic inhibition of SAA enhanced sensitivity to ICI plus TKI combination therapy, while blockade of the CEACAM1–TIM-3 axis in humanized PD-1 mouse models significantly potentiated anti–PD-1 efficacy. Our study establishes a single-cell atlas of the aRCC tumor microenvironment under treatment pressure and identifies a previously unrecognized SAA–CEACAM1–TIM-3 axis driving drug resistance, highlighting potential targets to improve therapy efficacy.

Renal cell carcinoma (RCC) accounts for approximately 2–3% of adult malignancies worldwide, with clear cell RCC (ccRCC) representing 70–80% of cases[1]. Around 30% of patients present with metastatic disease, and 20–40% of those with localized tumors experience recurrence post-nephrectomy[2]. Advanced RCC (aRCC) remains a lethal disease with a 5-year survival rate of only 11.7%[3]. The discovery of von Hippel–Lindau mutations and the central role of angiogenesis in ccRCC led to the establishment of tyrosine kinase inhibitors (TKIs) as first-line therapy[4]. Meanwhile, the immune-rich and pro-inflammatory nature of ccRCC supports the use of immune checkpoint inhibitors (ICIs). Recently, combination therapy with TKIs and ICIs has transformed aRCC treatment, achieving survival benefits in both advanced[2] and neoadjuvant settings[5].

However, drug resistance remains a major clinical challenge, with 5–20% of patients failing to respond to combination therapies[2]. Current clinical tools fail to reliably identify patients at risk of resistance. Traditional ICI biomarkers, including PD-L1, tumor mutational burden, and microsatellite instability, have limited utility in ccRCC. Transcriptomic studies in aRCC have revealed molecular subtypes associated with differential response—such as effector T cell and angiogenic signatures—but these findings require further validation[6].

A deeper understanding of the dynamic, multifactorial mechanisms underlying resistance, particularly the complex cellular crosstalk within the tumor microenvironment (TME), is essential for precision intervention. Single-cell RNA sequencing (scRNA-seq) offers an unprecedented opportunity to dissect TME heterogeneity and track

[1]Senior Department of Urology, Chinese PLA General Hospital, Beijing, China. [2]National Engineering Research Center of Ophthalmology and Optometry, Eye Hospital, Wenzhou Medical University, Wenzhou, China. [3]Medical School of Chinese PLA, Beijing, China. [4]Department of Urology, The Seventy-third Group Army Hospital, Xiamen, China. [5]School of Medicine, Nankai University, Tianjin, China. [6]These authors contributed equally: Liangyou Gu, Qi Zhang, Qiyang Liang, Cheng Peng, Yaohui Wang. ✉e-mail: dr.huangyan301@foxmail.com; xzhang301@163.com; mxin301@126.com; ciwm@foxmail.com; baojun40009@126.com

treatment-induced changes across cell types. Yet, an integrated single-cell–level analysis of resistance mechanisms in aRCC is lacking.

Here, we conduct comprehensive scRNA-seq analyses on 61 tumor samples from 34 aRCC patients treated with TKIs alone or in combination with ICIs. Our analyses reveal a previously unrecognized SAA^+ tumor–$CEACAM1^+$ neutrophil–$CD8^+$ T cell axis that promotes immune suppression and therapeutic resistance. These findings provide a mechanistic framework for treatment failure and nominate actionable targets to overcome resistance in aRCC.

Results

TME dynamics before and after ICI plus TKI combination therapy in aRCC

We performed scRNA-seq on tumor samples from 18 patients in the PLAGH cohort, including three treated with TKI monotherapy, and 15 with ICI plus TKI combination therapy. A total of 30 tumor samples were analyzed: nine were pre-treatment samples (six from non-responders [PreNR], three from responders [PreR]) and 21 post-treatment samples (17 from non-responders [PostNR], four from responders [PostR]). The samples were obtained from primary tumors ($n = 17$), tumor thrombi ($n = 9$), adrenal metastatic lesion ($n = 1$) or mixed tissue ($n = 3$). One post-treatment sample (P6) was excluded due to poor sequencing quality (Supplementary Datasets 1, 2).

To improve the analytical robustness of our study, we integrated two publicly available scRNA-seq datasets of aRCC. The first (HRA004711)[7], including tumor and adjacent normal tissues from four patients treated with TKI monotherapy and the second (GSE264586)[8], included samples from 12 patients treated with combination therapy, encompassing both primary and metastatic sites (Fig. 1a). After integration, the samples were classified as PreNR ($n = 17$), PreR ($n = 8$), PostNR ($n = 26$), and PostR ($n = 10$). After quality control, we profiled 333,169 high-quality single cells and constructed a comprehensive aRCC atlas, capturing the dynamic transcriptomic landscape across treatment (Fig. 1b, Supplementary Fig. 1a). Unsupervised clustering identified nine major cell types (Supplementary Dataset 3): normal epithelial cells ($n = 5544$; Supplementary Dataset 4), tumor cells ($n = 91{,}451$), T/NK cells ($n = 92{,}929$; Supplementary Dataset 5), B cells ($n = 10{,}407$; Supplementary Dataset 6), plasma cells ($n = 4508$; Supplementary Dataset 6), monocytic cells ($n = 78{,}895$; Supplementary Dataset 7), neutrophils ($n = 14{,}779$; Supplementary Dataset 8), mast cells ($n = 2303$; Supplementary Dataset 9), and stromal cells ($n = 32{,}353$; Supplementary Dataset 10), based on canonical marker genes (Supplementary Fig. 1b–i and; Supplementary Datasets 3–10).

Clinical trials including KEYNOTE-426, CheckMate 9ER, and RENOTORCH have demonstrated the superior efficacy of ICI plus TKI combination therapy compared to TKI monotherapy[2]. We compared changes in the proportions of major immune cell populations before and after treatment under these two therapeutic strategies. Notably, T cells, natural killer (NK) cells, B cells, plasma cells, and neutrophils exhibited distinct shifts in abundance. Neutrophils decreased following TKI monotherapy but increased with combination therapy (Supplementary Fig. 2a). A similar pattern was also observed for B cells and plasma cells (Supplementary Fig. 2a). In contrast, NK cells increased after TKI monotherapy but declined with combination therapy (Supplementary Fig. 2a). T cells increased after both treatments, especially in the combination group (Supplementary Fig. 2a). Within this group, responders had greater T cell enrichment, while macrophages and neutrophils were more predominant in non-responders (Supplementary Fig. 2b, c). Notably, responders exhibited higher T cell infiltration and reduced infiltration of myeloid cells across both treatment regimens (Supplementary Fig. 2b, c).

To quantify associations between immune cell populations and treatment outcomes, we applied a predictive index (Pi) and therapeutic index (Ti) frameworks[9]. T cells had the highest Pi, while neutrophils had the lowest (Fig. 1c). This finding was supported by multiplex immunohistochemistry (mIHC) staining, which revealed elevated neutrophil infiltration in the PreNR group (Fig. 1d). Across multiple RCC cohorts receiving ICI monotherapy, TKI monotherapy, or combination therapy, higher neutrophil signature scores were associated with shorter overall and progression-free survival (Supplementary Fig. 2d).

Ti analysis also associated B cells and plasma cells with favorable treatment responses, in line with previous studies[10,11]. Conversely, macrophages and neutrophils were consistently enriched in non-responders (Fig. 1c). Notably, macrophage enrichment in resistant RCC has been previously reported[12]. Neutrophils were also enriched in the PostNR group in our cohorts (Fig. 1d), and the same patterns were also observed when comparing major pathologic response (MPR) and non-MPR (NMPR) obtained from the post-treatment samples in the non-small cell lung cancer (NSCLC) dataset (Supplementary Fig. 2e–g).

In summary, our findings reveal significant alterations in the TME landscape of aRCC patients undergoing TKI monotherapy or ICI plus TKI combination therapy. Specifically, these results suggest the involvement of neutrophils, which may potentially contribute to therapeutic resistance in aRCC patients.

Distinct neutrophils confer resistance to TKI with or without ICI

Tumor-associated neutrophils have been linked to immunotherapy resistance, with higher infiltration predicting poorer survival[13]. A pan-cancer analysis also revealed substantial transcriptional heterogeneity among neutrophils[14]. We performed high-resolution profiling of intratumoral neutrophils and identified six transcriptionally distinct subclusters: Neu_01_S100A8, Neu_02_CD74, Neu_03_Stress, Neu_04_ZFP36L1, Neu_05_IRF1, and Neu_06_VEGFA (Fig. 1b, Fig. 2a, and Supplementary Fig. 1i). The Neu_01_S100A8 exhibited enrichment in chemotaxis-related pathways and high expression of *S100A12* (Supplementary Figs. 1i, 3a–b), resembling previously characterized $S100A12^+$[14] and $CD10^+ALPL^+$ neutrophils[15]. The Neu_02_CD74 displayed elevated *CD74* expression and enrichment in antigen presentation pathways (Supplementary Figs. 1i, 3a, b), consistent with the $HLA\text{-}DR^+CD74^+$ neutrophils associated with favorable prognosis and improved PD-1 response[14]. The Neu_05_IRF1 expressed the immune checkpoint molecule *CD274* (Fig. 2b), aligning with the $PD\text{-}L1^+$ TANs that suppress T cell cytotoxicity[16] (Supplementary Figs. 1i, 3a, b). Notably, the Neu_06_VEGFA subcluster ($VEGFA^+$ neutrophils) expressed high expression of *VEGFA*, *CXCR4*, and *LDHA* (Fig. 2b), with enrichment in glycolysis and hypoxia-related pathways, similar to the $VEGFA^+SPP1^+$ neutrophils linked to poor prognosis[14] (Fig. 2c, Supplementary Fig. 3a). This subset also exhibited high *CXCR4* expression (Fig. 2b), consistent with $CXCR4^{hi}$ neutrophils characterized by increased neutrophil extracellular traps (NETs) formation and inflammatory cytokine production, accompanied by lactate-driven vascular remodeling[17].

After treatment, responders exhibited reduced proportions of Neu_01_S100A8, Neu_06_VEGFA, Neu_04_ZFP36L1, Neu_05_IRF1, and Neu_03_Stress, but a higher proportion of Neu_02_CD74 than non-responders (Supplementary Fig. 3c). Notably, while Neu_06_VEGFA was enriched in responders prior to treatment, its expansion was predominantly observed in non-responders after treatment (Supplementary Fig. 3c). This post-treatment enrichment was further validated by mIHC (Fig. 2d). Trajectory analysis revealed two primary differentiation routes from Neu_01_S100A8 towards either Neu_02_CD74 or Neu_06_VEGFA. Neutrophils predominantly differentiated along the Neu_02_CD74 lineage in responders and the Neu_06_VEGFA lineage in non-responders (Supplementary Fig. 3d–g). Pi and Ti analyses further supported these observations, with Pi identifying Neu_01_S100A8 as a baseline predictor of poor response, and Ti highlighting Neu_06_VEGFA as a treatment-associated mediator of therapeutic resistance (Fig. 2e). To assess neutrophil reprogramming following therapy, we compared the transcriptional profiles between PostR and PostNR

https://doi.org/10.1038/s41467-026-70978-z

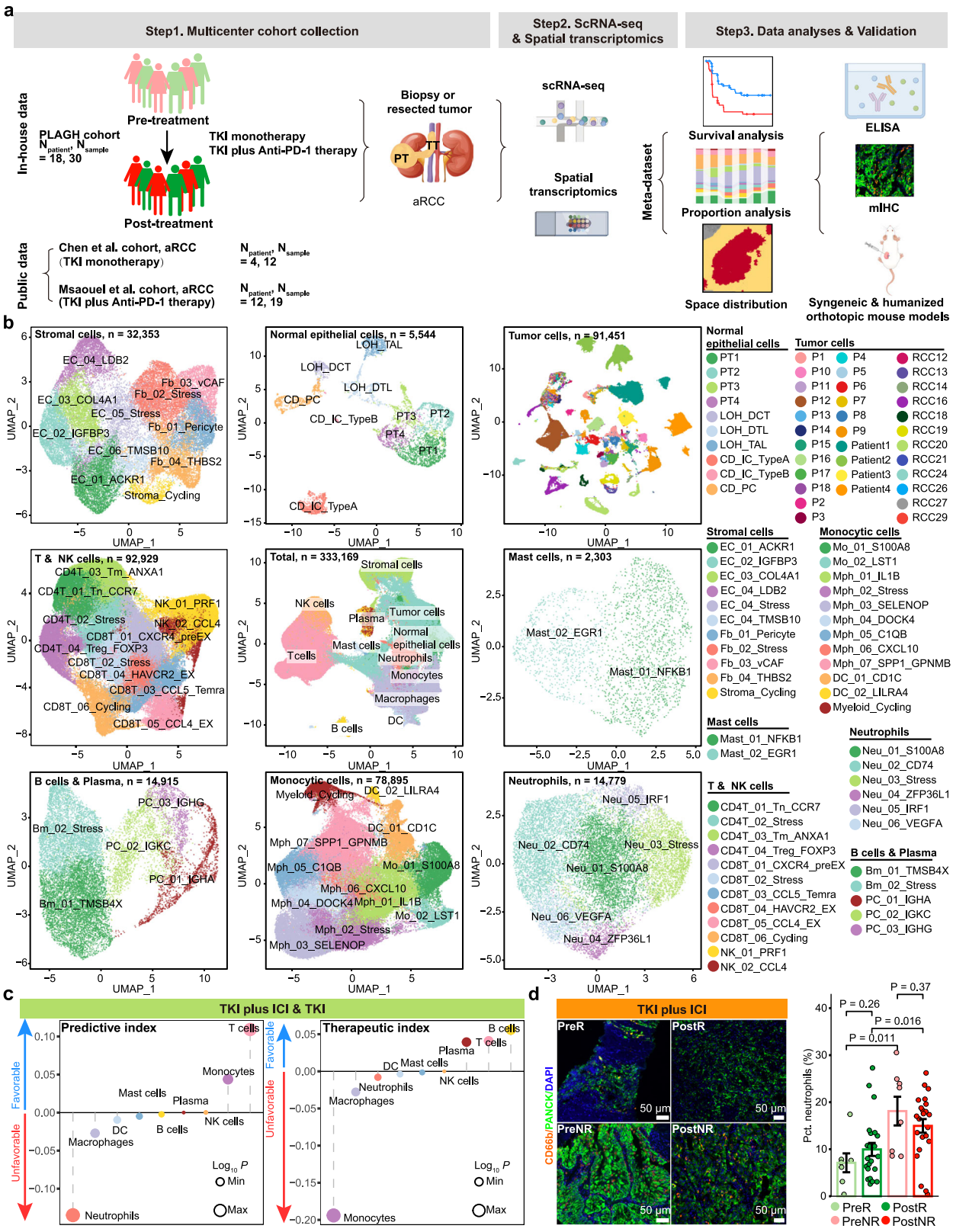

samples. Neutrophils from PostNR samples exhibited upregulation of immune checkpoints including carcinoembryonic antigen-related cell adhesion molecule 1 (*CEACAM1*), *VSIG4* and *CD300A* (Fig. 2f, Supplementary Dataset 11), along with enrichment of pathways related to angiogenesis, neutrophil chemotaxis and negative regulation of T cell-mediated immunity (Fig. 2g). Among all neutrophil subclusters, Neu_06_VEGFA showed the highest expression of *LGALS3* and *CEACAM1* (Fig. 2b, h)—ligands for LAG-3 and TIM-3, respectively, which are predominantly expressed on CD8$^+$ T cells[18]. *LGALS3* is widely expressed in the TME, including normal epithelial cells, tumor cells, monocytes, macrophages and mast cells[19] (Supplementary Fig. 3h), its elevated expression in the Neu_06 subset likely reflects an acquired, stress-induced phenotype rather than a canonical neutrophil lineage marker. In contrast, *CEACAM1* is mainly expressed in neutrophils and

Fig. 1 | TME dynamics before and after TKI with/without ICI therapy in aRCC. **a** A schematic description of the overall study design and workflow. PT, primary tumor; TT, tumor thrombus; mIHC, multiplex immunohistochemistry. **b** UMAP visualization of 333,169 high-quality single cells across all samples, colored by cell type. Nine major cell populations were identified: T/NK cells ($n = 92,929$), tumor cells ($n = 91,451$), monocytic cells ($n = 78,895$), stromal cells ($n = 32,353$), neutrophils ($n = 14,779$), B cells ($n = 10,407$), normal epithelial cells ($n = 5544$), plasma cells ($n = 4508$), and mast cells ($n = 2303$). Here, "n" represents the number of single cells that passed quality control and were included in the analysis. **c**, Pi and Ti analysis across immune cell types. Dot size reflects statistical significance, defined as $-\log_{10}$ (p value). P value by two-sided Wald test. **d** left panel, mIHC images showing CD66b$^+$ neutrophils (orange), tumor cells (green), and nuclei (DAPI, blue) in pre-/post-treatment tumor tissues. Scale bars, 50 μm. Right panel, quantification of infiltration in PreNR ($n = 8$), PreR ($n = 7$), PostNR ($n = 23$), and PostR ($n = 23$) groups. P values were calculated using an unpaired two-sided t-test. Data are presented as mean ± standard error of the mean (SEM).

endothelial cells and is a key component of NETs[20,21] (Fig. 2h, Supplementary Fig. 3i), underscoring its subset specificity and immunomodulatory relevance in resistance-associated neutrophils. Disruption of CEACAM1–TIM-3 interactions has been shown to enhance PD-1 efficacy[22,23]. Given these observations, we investigated the association of *CEACAM1*$^+$ neutrophils with non-responsiveness. In our cohort and three additional pan-cancer datasets, including NSCLC and colorectal cancer (CRC), *CEACAM1*$^+$ neutrophils were significantly enriched in the PostNR group (Fig. 2i, Supplementary Fig. 3j–m), a finding further validated by mIHC (Fig. 2j). Post-treatment bulk RNA-seq revealed elevated *CEACAM1* expression in non-responders, suggesting its association with hepatocellular carcinoma (HCC) treated with ICI plus TKI (Fig. 2k)

We identified distinct neutrophil subpopulations linked to resistance against both TKI monotherapy and ICI plus TKI therapy. Among them, Neu_06_VEGFA stood out as a key immunosuppressive subset, potentially mediating resistance through CEACAM1–driven immunomodulatory effects.

SAA$^+$ tumor cells associated with resistance to TKI with or without ICI

Tumor cells, as central components of the TME, play a pivotal role in shaping immune responses. Accumulating evidence demonstrates that tumor-derived signals recruit neutrophils, thereby fostering an immunosuppressive niche that facilitates tumor progression and therapy resistance[24]. To investigate the source of neutrophil recruitment in aRCC, we reconstructed cellular interaction networks through ligand-receptor analysis. In non-responders with aRCC, monocytes, macrophages and dendritic cells more frequently expressed the chemokines (*CXCL2*, *CXCL3* and *CXCL8*) to recruit *CXCR2*$^+$ neutrophils compared to those in responders (Fig. 3a). Notably, tumor cells from post-treatment non-responders exhibited increased expression of *CXCL14*, a chemokine known to recruit *CXCR4*$^+$ neutrophils[25] (Fig. 3a). This is consistent with the Neu_06_VEGFA enrichment seen in PostNR samples (Fig. 2d).

To compare the differences in the cellular states of malignant cells between postR and postNR groups, we directly compared malignant cells from these two groups treated with ICI plus TKI to identify differentially expressed genes (DEGs) (Fig. 3b, Supplementary Dataset 12). Notably, ferroptosis-inhibiting genes like *SLC7A11* were enriched in malignant cells from the postNR group (Fig. 3b). Their upregulation, driven by interleukin 6 via the JAK2–STAT3 pathway, was previously reported in patients with aRCC receiving TKI monotherapy[7]. Our data indicate that the same pathway is activated during combination therapy, potentially driving resistance in non-responders. DEGs were also significantly enriched in pathways associated with acute inflammatory response and neutrophil infiltration, including *SAA1* and *SAA2* (Fig. 3b, c).

Dimensionality reduction clustering of aRCC malignant cells revealed substantial inter-patient heterogeneity (Fig. 1b). To identify conserved functional programs while minimizing transcriptional variability driven by gene dosage effects, we applied non-negative matrix factorization. This approach defined nine metaprograms (MPs) in malignant cells, which were subsequently annotated into eight functional modules based on signature genes and enriched pathways (Fig. 3d, Supplementary Fig. 4a, b and Supplementary Dataset 13). These modules corresponded to: (1) cell cycle (MP1; *TOP2A* and *STMN1*), (2) neuronal-like[26] (MP2; *NR2F2* and *PTPRG*), (3) chemokines regulation (MP3; *CXCL1* and *CXCL2*), (4) Proximal tubule (MP4; *NAT8* and *SLC17A3*), (5) epithelial-mesenchymal transition I (EMT I, MP5; *LOX*, *PLOD2* and *TGM2*), (6) EMT II (MP6; *SAA1*, *SAA2* and *CXCL14*), (7) MHC-II (MP7; *CD74* and *HLA-DPA1*), and (8) stress response processes (MP8; *HSP90AA1* and *HSPA1A*). Module similarity analysis between our aRCC cohort and a recent study of treatment-naive RCC[27] revealed strong concordance, suggesting that the functional architecture of tumor programs is largely preserved following treatment (Supplementary Fig. 4b). External validation of these findings using the TCGA-KIRC cohort confirmed a significant association between the activity of MP1, MP4, MP5, and MP6 tumor cell signatures and both overall survival and progression-free survival in patients with ccRCC (Supplementary Fig. 4c).

We annotated MP5 and MP6 as EMT-related modules based on their strong enrichment for hypoxia and EMT pathways (Supplementary Fig. 4a). MP5 incorporates extracellular matrix (ECM)-mediating factors, including *LOX, PLOD2*, *TGM2* and is enriched in functions related to ECM organization (Fig. 3d). Its expression was significantly elevated in post-treatment samples compared to pre-treatment ones and was notably higher in PreNR tumor cells than in PreR cells (Fig. 3e). Additionally, MP6 contains *SAA1*, *SAA2*, *CXCL14*, and is enriched in functions related to the acute phase response, neutrophil chemotaxis, and migration (Supplementary Fig. 4a). Tumor cell scoring across our dataset and external single-cell datasets showed that MP6 was significantly upregulated in PostNR samples compared to PostR (Fig. 3e).

To further investigate tumor cell-intrinsic drivers of drug resistance in aRCC, we intersected genes from the postNR-enriched MP6 module with those consistently upregulated in both postNR samples and TKI-resistant ccRCC cell lines (A-498 and 786-O), identifying *SAA1* and *SAA2* as shared candidates (Fig. 3f and Supplementary Datasets 14, 15). Serum amyloid A (SAA, comprising the SAA1/SAA2 isoforms in humans) is rapidly induced during acute-phase inflammatory responses[28], and has been implicated in immune suppression and RCC progression[29–31]. Transcriptomic data from patients with HCC receiving ICI plus TKI therapy revealed higher *SAA* expression in postNR versus postR samples (Fig. 3g), suggesting a broader role for SAA in mediating resistance across cancers. Moreover, we validated that high *SAA* expression was significantly associated with poor survival outcomes in five previously published pan-cancer ICI datasets (Fig. 3i, Supplementary Fig. 4d, e). To assess the clinical utility of SAA as a predictive biomarker for ICI plus TKI therapy, we performed enzyme-linked immunosorbent assay-based quantification of pre-treatment plasma samples and found significantly elevated circulating SAA levels in patients with preNR tumors (Fig. 3j). At the tissue level, mIHC revealed increased SAA$^+$ tumor cell abundance not only in preNR compared to preR samples, but also in post-treatment samples relative to pre-treatment, suggesting that therapy may further amplify the SAA$^+$ tumor cell population enriched in NR groups (Fig. 3h). This enrichment was further confirmed in postNR versus postR tumors by both mIHC and scRNA-seq analyses (Fig. 3h; Supplementary Fig. 4f).

https://doi.org/10.1038/s41467-026-70978-z

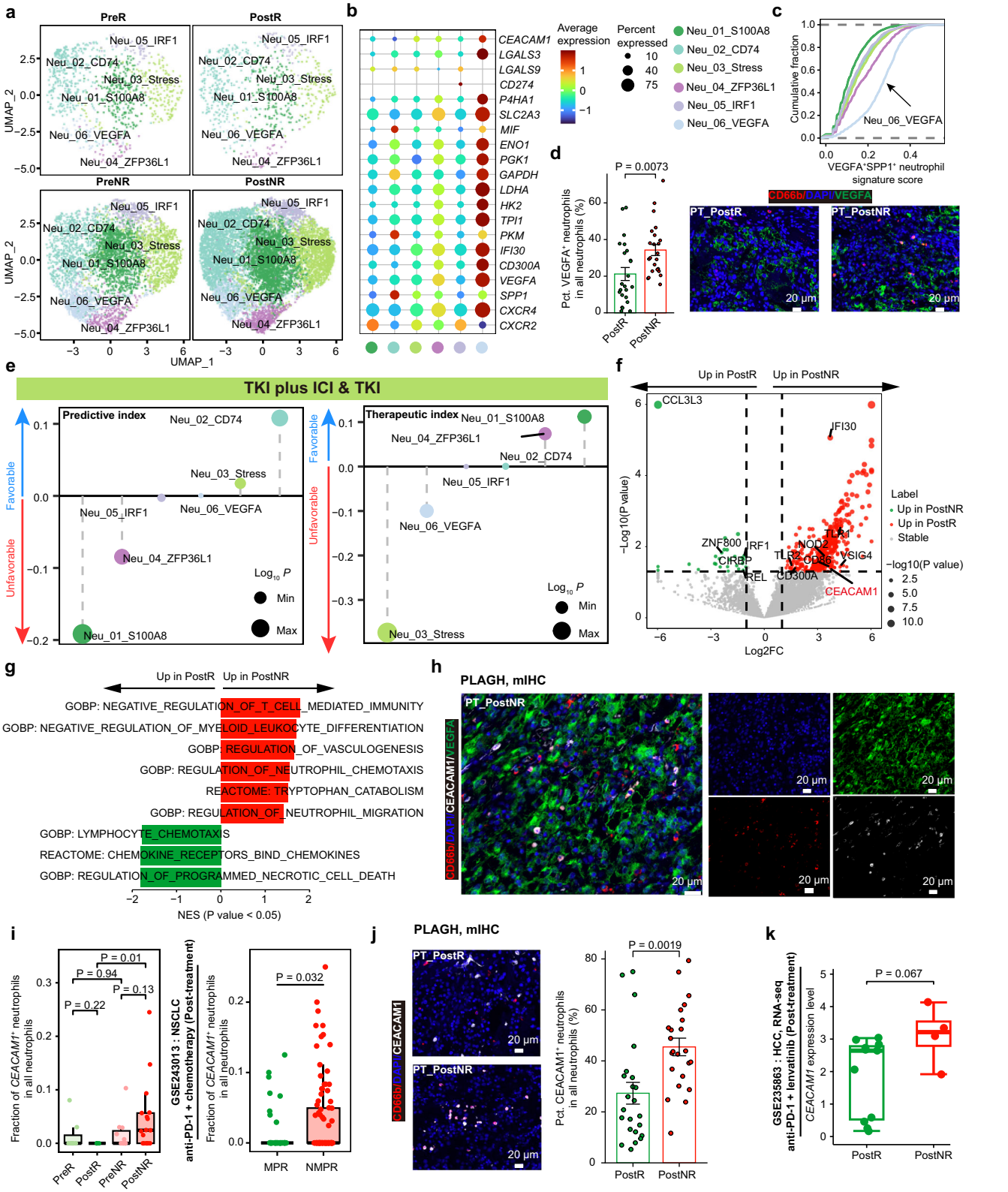

Collectively, these findings suggest that SAA$^+$ tumor cells may constitute a persistent, treatment-amplified resistance population in aRCC.

SAA blockade enhances the combination therapy efficacy

SAA has been demonstrated to induce PD-L1 expression in neutrophils via LDHA/STAT3-mediated glycolytic activation and oncostatin M release, thereby attenuating cytotoxic T cell function in HCC[32]. Our data revealed significant enrichment of SAA$^+$ tumor cells and Neu_06_VEGFA in PostNR tumors, suggesting a symbiotic regulatory dynamic between these cell types. To clarify the spatial relationship between *SAA*$^+$ tumor cells and *VEGFA*$^+$ neutrophils, we divided TME into tumor core and margin (Supplementary Fig. 5a–f). In non-responders, *SAA*$^+$ cells mainly localize in the core with a few scattered in the margin, where *VEGFA*$^+$ neutrophils are enriched (Supplementary Fig. 5g, h). Co-localization index analysis showed non-responders have

Fig. 2 | Distinct neutrophil subsets and their phenotypic dynamics in response to TKI or ICI plus TKI therapy. a UMAP plots showing six transcriptionally distinct neutrophil subclusters across responder and non-responder groups before and after treatment. **b** Dot plot of average gene expression and percentage of cells expressing selected neutrophil marker genes across subclusters. Dot size represents the percentage of cells expressing the gene, and color indicates the scaled mean expression. **c** UCell scores of neutrophil subsets based on a *VEGFA*$^+$*SPP1*$^+$ signature. **d** Quantification of the percentage of VEGFA$^+$ neutrophils among all neutrophils in PostNR ($n = 23$), and PostR ($n = 23$) groups (left), and representative mIHC images of VEGFA$^+$ neutrophils (right); Scale bars, 20 μm. *P* value by unpaired two-sided *t*-test. Data as mean ± SEM. **e** Pi and Ti analysis of neutrophil subclusters in TKI or ICI plus TKI tumors. Dot size represents the significance evaluated by $-\mathrm{Log}_{10}$ (*p* value). *P* value by two-sided Wald test. **f** Volcano plot comparing gene expression between neutrophils from post-treatment responder and non-responder tumors; Selected upregulated genes labeled. *P* value by Wald test in DESeq2. **g** GSEA of pathways upregulated in neutrophils from post-treatment responder or non-responder tumors; NES, normalized enrichment scores. Adaptive multi-level split Monte Carlo scheme. **h** Representative mIHC images showing Neu_06_VEGFA in postNR in the PLAGH cohort; Scale bars, 20 μm. **i** Fraction of *CEACAM1*$^+$ neutrophils in total neutrophils across cohorts. Left: our study (PreNR, $n = 11$; PreR, $n = 7$; PostNR, $n = 17$; PostR, $n = 3$). Right: NSCLC cohort (GSE243013; MPR, $n = 38$; NMPR, $n = 93$). *P* value by unpaired two-sided *t*-test. **j** Representative mIHC images and quantification of CEACAM1$^+$ neutrophils in responder and non-responder tumors in the PLAGH cohort; Right panel, quantification of CEACAM1$^+$ neutrophil infiltration in PostNR ($n = 23$), and PostR ($n = 23$) groups. Scale bars, 20 μm. *P* value by unpaired two-sided *t*-test. Data as mean ± SEM. **k** *CEACAM1* expression levels in bulk RNA-seq data of post-treatment HCC samples (GSE235863; PostR, $n = 11$; PostNR, $n = 4$). *P* value by unpaired two-sided *t*-test.

higher indices than responders, supporting their potential interaction in non-responders' tumor margin (Supplementary Fig. 5i). Furthermore, cell–cell communication analysis revealed enhanced interactions between *SAA*$^+$ tumor cells and Neu_06_VEGFA in PostNR samples (Supplementary Fig. 6a). To functionally validate the SAA–CEACAM1 axis, we performed an in vitro perturbation experiment showing that SAA stimulation upregulates CEACAM1 expression in neutrophils (Fig. 4a, b; Supplementary Fig. 6b). Given the symbiotic interaction between *SAA*$^+$ tumor cells and *VEGFA*$^+$ neutrophils, we evaluated the therapeutic potential of targeting this axis in RCC. In preclinical syngeneic orthotopic RCC mouse models, triple therapy combining anti-SAA1/2 antibody, axitinib, and anti–PD-1 antibody produced a synergistic antitumor effect (Fig. 4c, d), without causing notable toxicity and outperforming either anti–PD-1 plus axitinib or anti-SAA1/2 monotherapy (Fig. 4e). mIHC analysis demonstrated that triple therapy increased CD8$^+$ T cell infiltration (Fig. 4f) and significantly reduced neutrophil infiltration (Fig. 4g).

ScRNA-seq re-analysis of *Saa*$^{-/-}$ and wild-type (WT) mice[33], revealed 11 major cell types using canonical markers (Supplementary Fig. 6c, d). Focusing on neutrophils, we identified eight distinct subpopulations (Supplementary Figs. 6e, f). Among them, mNeu_07_Ldha demonstrated notably higher expression levels of both *Ldha* and *Hilpda* and exhibited a transcriptional pattern highly comparable to that of Neu_06_VEGFA (Supplementary Fig. 6f). A significantly higher proportion of mNeu_07_Ldha was observed in WT mice (Fig. 4h, i).

Neutrophils from WT mice exhibited upregulation of angiogenesis- and chemotaxis-related genes and pathways (Fig. 4j, Supplementary Fig. 6g). Moreover, CD8$^+$ T cells from *Saa*$^{-/-}$ mice exhibited enrichment in NK cell activation and immune-stimulatory pathways (Supplementary Fig. 6h). A comparison of transcriptomic differences between *Saa*$^{-/-}$ and WT neutrophils revealed upregulation of *Ceacam1* expression (Fig. 4j). Similarly, SAA blockade using an anti-SAA1/2 antibody led to elevated *Ceacam1* expression in neutrophils within the orthotopic RCC model (Fig. 4k).

Collectively, *SAA*$^+$ tumor cells orchestrate a pro-tumor microenvironment by promoting Neu_06_VEGFA infiltration and CD8$^+$ T cell dysfunction.

Diverse T cells distinguish therapy sensitivity and resistance

Numerous studies have underscored the importance of T cell characteristics within the TME and their influence on the response to antitumor therapies[34]. Our mIHC data revealed increased infiltration of CD8$^+$ T cells in the PostR group following combination therapy (Fig. 5a). Conversely, a higher density of CD8$^+$ T cells was observed in the PreNR group prior to treatment (Fig. 5a). This observation aligns with our previous report, in which biopsy specimens from non-responders exhibited enhanced infiltration of CD8$^+$ cells[5]. Combination therapy also significantly enhanced T cell-mediated anti-tumor response activity in CD8$^+$ T cells compared to TKI monotherapy (Supplementary Fig. 7a, b). Using high-resolution T/NK cell profiling in aRCC tumors, we identified four CD4$^+$ T cell subsets, six CD8$^+$ T cell subsets, and two NK cell subsets (Fig. 1b; Supplementary Figs. 1d, 7c, d). The CD8$^+$ T cells were further classified into six subsets: cycling CD8$^+$ T cells (CD8T_06_Cycling, *MKI67*$^+$), memory-like CD8$^+$ T cells (CD8T_01_CXCR4_preEX, *TCF7*$^+$*CCR7*$^+$*CXCR4*$^+$), intermediate exhausted CD8$^+$ T cells (CD8T_03_CCL5_Temra, *GZMK*$^+$*CCL5*$^+$*CD74*$^+$, Exh-Pre), stress-state CD8$^+$ T cells (CD8T_02_Stress, *HSPA1A*$^+$, Exh-Prog), and two terminally exhausted subsets (CD8T_04_HAVCR2_EX, *CCL5*$^+$*ENTPD1*$^+$*HAVCR2*$^+$; Exh-Term and CD8T_05_CCL4_EX, *CCL4*$^+$*CCL4L2*$^+$*CCL5*$^+$, Exh-KLR) (Figs. 1b, 5b; Supplementary Figs. 1d, 7e, f)[35–37]. Trajectory and proportion analyses indicated that, compared to TKI monotherapy, combination therapy appeared to facilitate the transition from Exh-Pre to Exh-Prog (Supplementary Fig. 7g–j). However, in the PostNR group receiving combination therapy, Exh-Prog cells accumulated, suggesting a potential blockade in their progression to terminally exhausted states (Supplementary Fig. 7h). This finding is consistent with the previously described significant enrichment of the terminally exhausted gene signature in cells from responders compared to non-responders in RCC immunotherapy[35,38]. The CD4$^+$ T cells were reclustered into four subsets: naive CD4$^+$ T cells (CD4T_01_Tn_CCR7, *CCR7*$^+$), stress-state CD4$^+$ T cells (CD4T_02_Stress, *HSPA1A*$^+$), memory CD4$^+$ T cells (CD4T_03_Tm_ANXA1, *ANXA1*$^+$ *CD40LG*$^+$), and regulatory T cells (Tregs, CD4T_04_Treg_FOXP3, *FOXP3*$^+$) (Supplementary Figs. 1d, 7c, d). Compared to TKI monotherapy, combination therapy significantly increased the proportion of Tregs, particularly in the PostNR group (Supplementary Fig. 8a, b).

Previous studies have implicated TIM-3 and other immune checkpoints in adaptive resistance to PD-1 blockade[39]. Building on our findings of *CEACAM1* enrichment in neutrophils from PostNR tumors, we noted that its ligand, TIM-3 (*HAVCR2*), is predominantly expressed on CD8$^+$ T cells[23], prompting investigation of the CEACAM1–TIM-3 axis as a potential mediator of resistance. Across both therapeutic regimens, PD-1$^-$TIM-3$^+$ CD8$^+$ T cells were significantly enriched in PostNR samples (Fig. 5c, Supplementary Fig. 9a and Supplementary Datasets 16, 17). This finding was validated in three independent pan-cancer datasets (Fig. 5d, Supplementary Fig. 9b, c). PD-1$^-$TIM-3$^+$ CD8$^+$ T cells exhibited elevated exhaustion scores (second only to PD-1$^+$TIM-3$^+$ cells) and reduced PD-1 response signatures (Supplementary Fig. 9d, e). Consistent with the reduction of PD-1$^+$CD8$^+$ T cells after treatment, the relative enrichment of PD-1$^-$TIM-3$^+$ CD8$^+$ T cells suggests that TIM-3 upregulation, rather than sustained PD-1 signaling, represents the dominant exhaustion pathway in PostNR samples (Fig. 5c). Transcriptomic and pathway enrichment analyses demonstrated that TIM-3 upregulation was associated with enhanced immune evasion programs (Supplementary Fig. 9f–i) indicating a functional role for TIM-3 in adaptive resistance to PD-1 blockade.

https://doi.org/10.1038/s41467-026-70978-z

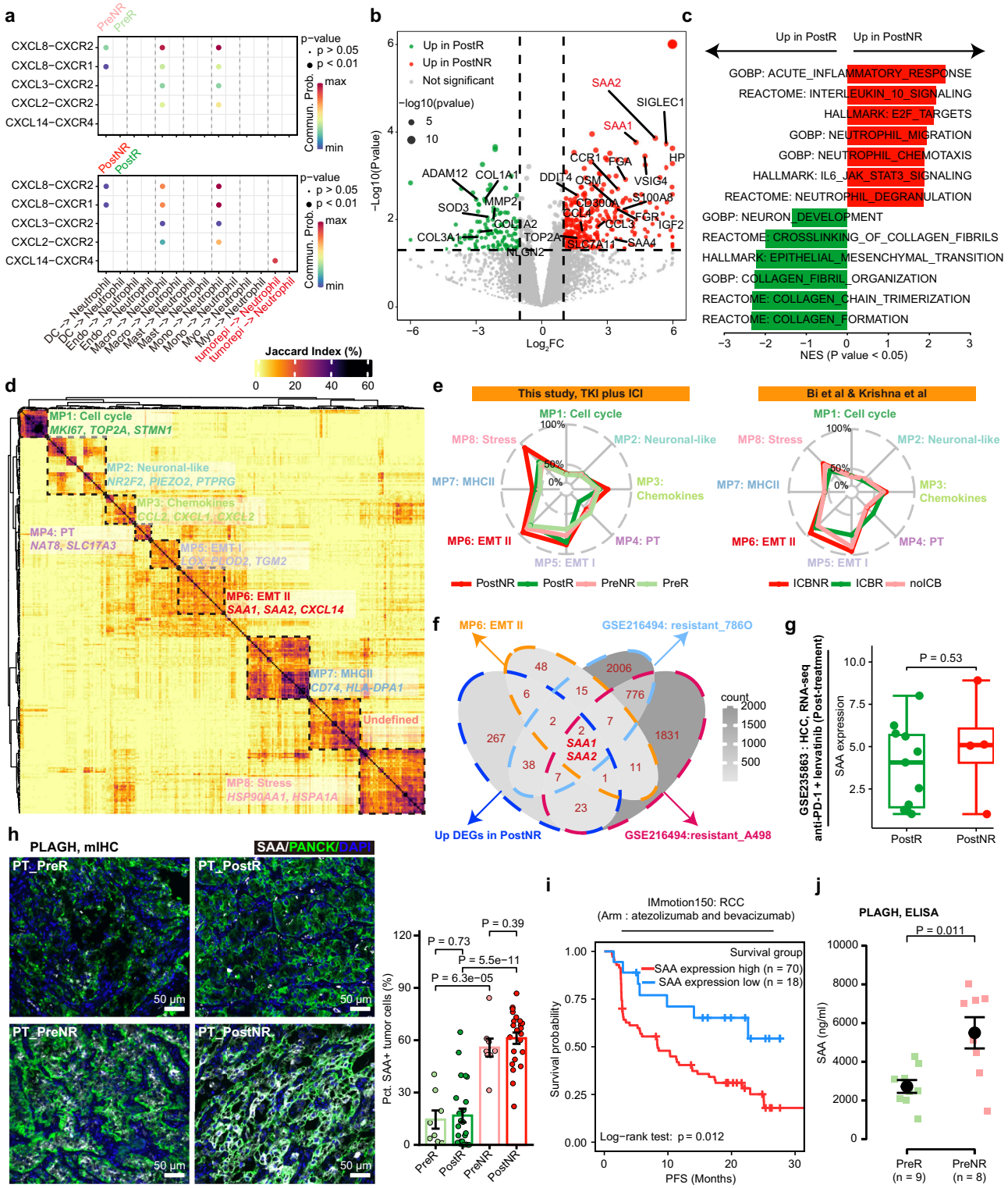

Notably, spatial transcriptome-based cell abundance analysis revealed the co-occurrence of Neu_06_VEGFA and CD8$^+$ T cell subsets (Fig. 5e, Supplementary Fig. 10a). Specifically, Neu_06_VEGFA and PD-1$^-$TIM-3$^+$ CD8$^+$ T cells exhibited spatial co-localization across multiple samples (Fig. 5e, Supplementary Fig. 10a). Intriguingly, in PostNR samples, Neu_06_VEGFA cells were positioned significantly closer to PD-1$^-$TIM-3$^+$ CD8$^+$ T cells than in PostR samples (Fig. 5e, Supplementary Fig. 10a). This observation was further supported by a higher co-localization index between these two populations in PostNR samples (Supplementary Fig. 10b), indicating a preferential spatial association of Neu_06_VEGFA with PD-1$^-$TIM-3$^+$ CD8$^+$ T cells in non-responders. Considering the limitations of low-resolution in Visium spot-level data, we further analyzed scRNA-seq data and found enhanced interactions between Neu_06_VEGFA and PD-1$^-$ TIM-3$^+$ CD8$^+$ T cells (Fig. 5f, g). NicheNet analysis indicated that Neu_06_VEGFA may promote exhaustion in PD-1$^-$TIM-3$^+$ CD8$^+$ T cells by upregulating the expression of exhaustion-associated transcription factors *BHLHE40*, *PRDM1*, and *STAT3* via *CEACAM1-HAVCR2* signaling (Fig. 5h).

In summary, combination therapy enhances CD8$^+$ T cell infiltration but also accelerates their progressive exhaustion, especially in

Fig. 3 | Tumor-intrinsic *SAA*$^+$ metaprogram contributes to resistance to TKI with or without ICI therapy. a Ligand–receptor interaction analysis reveals neutrophil-attracting chemokines (*CXCL2*, *CXCL3*, *CXCL8*, and *CXCL14*) expressed by other cells. The color and size of the dots represent the calculated communication probability and the corresponding *P* values (one-sided permutation test), respectively. **b** Volcano plot showing DEGs between tumor cells from PostR and PostNR samples. Selected upregulated genes labeled. Wald test in DESeq2 was used to determine *P* values. **c** GSEA of pathways upregulated in tumor cells from post-treatment non-responders compared to responders; NES, normalized enrichment scores. Statistical analysis was performed using an adaptive multi-level split Monte Carlo scheme. **d** Heatmap of the nine NMF-derived metaprograms (MPs) and their corresponding gene modules in tumor cells. **e** Radar plots showing metaprogram scores (MP5 and MP6) across treatment groups in our aRCC cohort, as well as two additional ccRCC single-cell datasets. **f** Venn diagram showing overlap of MP6 genes with genes upregulated in PostNR tumor cells and in TKI-resistant ccRCC cell lines (A-498 and 786-O). **g** Box plots showing *SAA* expression in HCC tumors from patients receiving ICI plus TKI therapy (GSE235863; PostR, $n = 11$; PostNR, $n = 4$). *P* values were calculated using an unpaired two-sided *t*-test. **h** Representative mIHC images and quantification of SAA$^+$ tumor cells in responder and non-responder tumors across pre-/post-treatment groups in the PLAGH cohort; right panel, quantification of SAA$^+$ tumor cell abundance in PreNR ($n = 8$), PreR ($n = 7$), PostNR ($n = 23$) and PostR ($n = 23$) groups. Scale bars, 50 μm. *P* values were calculated using an unpaired two-sided *t*-test. Data are presented as mean ± SEM. **i** Kaplan–Meier analysis of progression-free survival (PFS) in IMmotion150 cohorts stratified by *SAA* expression levels. *P* values were calculated using the log-rank test. **j** Circulating SAA levels in pre-treatment plasma from PreR ($n = 9$) and PreNR ($n = 8$) patients in PLAGH measured by ELISA. *P* values were calculated using an unpaired two-sided *t*-test. Data are presented as mean ± SEM.

non-responders. The accumulation of Tregs and Exh-Prog CD8$^+$ T cells fosters a more immunosuppressive TME following combination therapy. Our results indicate that the CEACAM1–TIM-3 axis serves as a crucial driver of adaptive resistance, providing a potential therapeutic target to improve treatment efficacy.

CEACAM1–TIM-3 blockade alleviates anti–PD-1 resistance

CEACAM1 mediates immune evasion during the precancerous stage of lung adenocarcinoma (LUAD) via TIM-3 binding, and that TIM-3 blockade can attenuate tumor progression[40]. Notably, the anti-CEACAM1 monoclonal antibody exhibits synergistic anti-tumor activity with anti–PD-1 in NSCLC[41], aligning with reports that disrupting CEACAM1–TIM-3 interactions enhances the efficacy of PD-1 blockade[22,23]. To evaluate the therapeutic potential of this axis, we utilized a humanized PD-1 mouse model bearing orthotopic murine RCC tumors, which inherently display resistance to PD-1 monotherapy[42]. ML-T7, a CEACAM1–TIM-3 blocking agent[43], effectively suppressed tumor growth both as monotherapy and in combination with the human anti–PD-1 antibody Toripalimab (Fig. 6a–c). While Toripalimab monotherapy alone had no effect on tumor regression, the combination therapy achieved superior tumor control, with no significant weight loss, indicating a favorable safety profile (Fig. 6a–c). These findings are in line with previous studies in liver cancer, which showed that blockade of the CEACAM1–TIM-3 axis enhances the efficacy of PD-1 inhibition[22].

To explore the mechanism by which TIM-3 blockade overcomes PD-1 resistance in RCC, we conducted 10x GEM-X single-cell transcriptomic profiling on tumors harvested from mouse specimens (Fig. 6a). Unsupervised clustering identified 12 major cell types (Fig. 6d, Supplementary Fig. 10c and Supplementary Dataset 18). ML-T7 plus Toripalimab markedly reduced the proportion of *Ceacam1*$^+$ neutrophils compared to all other groups (Supplementary Fig. 10d), while increasing the proportion of Pd-1$^-$Tim-3$^+$ CD8$^+$ T cells relative to the control group (Supplementary Fig. 10d). In contrast, PD-1$^+$TIM-3$^+$ CD8$^+$ T cells were elevated in all treatment groups compared to the control (Supplementary Fig. 10d). This finding suggests that while combination therapy effectively targets myeloid-mediated immunosuppression, it does not fully prevent the accumulation of highly exhausted CD8$^+$ T cells co-expressing both checkpoints. Interestingly, differential abundance analysis revealed a significant enrichment of macrophages in the ML-T7 plus Toripalimab group compared to the control group, while neutrophils were predominantly enriched in the control group (Fig. 6e, f). Notably, the ML-T7 monotherapy group displayed a similar macrophage enrichment pattern to that of the combination therapy (Supplementary Fig. 10e, f). In contrast, CD4$^+$ T cells, CD8$^+$ T cells, and NK cells were more abundant in the control group relative to ML-T7 monotherapy (Supplementary Fig. 10e, f). Toripalimab monotherapy resulted in enrichment of CD4$^+$, CD8$^+$, and NK cells, as well as neutrophils, while showing macrophage infiltration patterns comparable to those of the control (Supplementary Fig. 10g, h).

To further investigate the effect of TIM-3 blockade on CD8$^+$ T cells, we compared exhaustion, oxidative phosphorylation (OXPHOS), and mitochondrial organization scores across treatment groups. CD8$^+$ T cells from the ML-T7 plus Toripalimab group exhibited significantly lower exhaustion and tolerance scores but higher OXPHOS and mitochondrial function scores than other groups (Fig. 6g), consistent with the known metabolic rewiring during T cell activation[44]. In contrast, Toripalimab monotherapy exhibited the highest exhaustion scores and upregulation of checkpoint genes like *Havcr2* and transcription factors such as *Stat3* and *Entpd1* (Fig. 6h). The combination treatment was enriched for mitochondrial metabolism genes including *Tpi1* and *Fabp5* (Fig. 6h).

Our results aslo showed that ML-T7 combined with Toripalimab markedly increased macrophage abundance (Fig. 6e, f). Further analysis revealed that macrophages from the combination group exhibited marked downregulation of genes associated with NLRP3 inflammasome activation relative to controls (Fig. 6i), accompanied by downregulation of key inflammasome genes such as *Nlrp3*, *Il1a*, and *Il1b* (Fig. 6j). These data are consistent with accumulating evidence that macrophage-intrinsic NLRP3 inflammasome activation drives tumor progression and undermines immunotherapeutic efficacy[45].

Collectively, the ML-T7 plus anti–PD-1 combination may overcome resistance by reinvigorating CD8$^+$ T cells and reducing myeloid-driven immunosuppression through inhibition of macrophage NLRP3 inflammasome activity.

Discussion

The immunosuppressive TME poses a significant obstacle to the effective use of TKIs, ICIs, and their combination in RCC, as evidenced by previous studies[12,38]. Overcoming this barrier requires both accurate stratification of patient responses and a mechanistic understanding of treatment resistance. In this study, we characterized the single-cell profiles of tumor cells and immune cells in samples obtained from patients with aRCC treated with TKIs with or without ICIs. We identified CD8$^+$ T cell enrichment as a hallmark of favorable response to combination therapy, whereas neutrophil abundance robustly predicted treatment failure. Notably, the expansion of VEGFA$^+$ neutrophils was strongly associated with resistance to combination therapy. Mechanistically, VEGFA$^+$ neutrophils upregulated the immune checkpoint ligand CEACAM1, thereby impairing CD8$^+$ T cell function. Importantly, we further identified selective enrichment of SAA$^+$ tumor cells in non-responders, which promoted the accumulation of VEGFA$^+$CEACAM1$^+$ neutrophils, thereby establishing an SAA–CEACAM1–TIM-3–mediated immunosuppressive axis that drives resistance to ICI plus TKI combination therapy in aRCC.

SAA isoforms 1 and 2 are acute inflammatory proteins induced during sepsis[28]. SAA has also been identified as a biomarker for resistance to anti–PD-1 antibody in NSCLC[46] and HCC[32]. Consistent with

https://doi.org/10.1038/s41467-026-70978-z

these reports, we observed tumor cell–specific overexpression of SAA in patients with intrinsic or acquired resistance to combination therapy. Importantly, non-responders exhibited significantly higher baseline plasma SAA levels prior to treatment than responders, supporting its potential as a predictive biomarker. Previous studies have indicated that SAA promotes an immunosuppressive TME[47] and is associated with TKI resistance[48] and poor prognosis[30] in RCC. However, its functional role within the RCC TME has remained poorly defined. A distinct tumor subset (Cluster 4), marked by high expression of *SAA1*, *SAA2*, and *APOL1*, has been linked to metastatic potential[29], suggesting a potential role in disease progression. Collectively, these findings support a dual role for SAA as both a clinically actionable biomarker and a driver of therapeutic resistance, and raise the possibility that targeting SAA may enhance immunotherapy efficacy while limiting treatment-associated tumor progression.

Importantly, our in vitro functional perturbation experiments show that SAA stimulation upregulates CEACAM1 expression in neutrophils. In parallel, based on our integrative single-cell, functional, and

Fig. 4 | SAA blockade improves the efficacy of combination therapy. **a** Representative flow cytometry histograms showing surface CD66a/c/e expression in human neutrophils following stimulation with increasing concentrations of recombinant human SAA for 12 h. **b** Quantification of relative *CEACAM1* expression levels assessed by flow cytometry (left) and qRT-PCR (right) under the indicated SAA concentrations. Each dot represents an independent sample ($n = 8$). *P* value by unpaired two-sided *t*-test. Data as mean ± SEM. **c** Schematic of the syngeneic orthotopic RCC mouse model treated with anti-SAA1/2 antibody, anti–PD-1 antibody, and axitinib ($n = 5$). **d** Representative images of tumors harvested from mice under each treatment condition ($n = 5$). **e** Quantification of tumor weight and body weight in the syngeneic orthotopic RCC model across four groups ($n = 5$). *P* value by unpaired two-sided *t*-test. Data as mean ± SEM. **f** Representative mIHC images and quantification of $CD8^+$ T cell infiltration in the syngeneic RCC orthotopic model across groups. Five independent biological replicates were included per group, with two regions of interest per sample (ROI, $n = 10$). Scale bars, 50 μm. *P* value by unpaired two-sided *t*-test. Data as mean ± SEM. **g** Representative mIHC images and quantification of neutrophil infiltration across groups. Five independent biological replicates were included per group, with two ROI per sample ($n = 10$). Scale bars, 50 μm. *P* value by unpaired two-sided *t*-test. Data as mean ± SEM. **h** Differences in the composition of the neutrophil population among subtypes in wild-type (WT) and *Saa*$^{-/-}$ mice (GSE232696). Fractions are visualized as cell density based on the UMAP embedding. **i** Relative abundance of neutrophil subpopulations across WT and *Saa*$^{-/-}$ mice (GSE232696). Color scale indicates relative enrichment ($R_{o/e}$). **j** Heatmap showing normalized expression of selected genes in neutrophils from WT and *Saa*$^{-/-}$ mice. Color scale represents gene expression intensity. **k** Proportion of *CEACAM1*$^+$ neutrophils in the RCC orthotopic mouse model under different conditions. Five independent biological replicates were included per group, with two ROI per sample ($n = 10$). *P* value by unpaired two-sided *t*-test. Data as mean ± SEM.

in vivo analyses, elevated CEACAM1 expression in neutrophils is associated with enhanced immunosuppressive activity, $CD8^+$ T cell exhaustion, and impaired cytotoxic function, collectively contributing to suboptimal response to combination therapy. CEACAM1 plays a crucial role in tumor immune evasion and metastasis, particularly through its association with NETs[49]. CEACAM1 also interacts with immune inhibitory receptors, such as TIM-3 on $CD8^+$ T cells, thereby exacerbating immune suppression within the TME[22,23,43]. Consistent with prior reports, our study further demonstrates that the CEACAM1–TIM-3 interaction is operational within the TME and contributes to immune dysfunction.

CEACAM1 is preferentially expressed in neutrophils and stromal cells and functions as a key immunomodulatory molecule. Although ICIs are intensively studied, efforts have focused mainly on established targets[50] such as PD-1, CTLA-4, TIGIT, and LAG-3. Research on CEACAM1 monoclonal antibodies remains limited, with most studies focusing on melanoma and NSCLC[41,51]. In NSCLC, the anti-CEACAM1 monoclonal antibody 3C11 has demonstrated synergistic anti-tumor activity when combined with anti–PD-1 therapy[41]. More recently, the CEACAM1-targeting antibody CM-24 has exhibited a favorable safety profile and encouraging antitumor activity in solid tumors, and is currently being evaluated in a phase II clinical trial in combination with nivolumab and chemotherapy for metastatic pancreatic cancer[52]. These findings provide a strong rationale for CEACAM1-directed immune re-challenge strategies in immune-refractory aRCC, particularly following failure of initial ICI plus TKI therapy.

Furthermore, we identified the CEACAM1–TIM-3 axis as a promising therapeutic target for resistance in RCC. Unlike SAA, a secreted acute-phase protein, CEACAM1 is a membrane-bound immune checkpoint, making it more amenable to antibody-based targeting. Although SAA inhibition enhanced the efficacy of ICI plus TKI therapy in an RCC mouse model, it concurrently induced compensatory CEACAM1 upregulation in neutrophils, indicating an adaptive immune escape mechanism. ScRNA seq data from the *Saa*$^{-/-}$ mouse model also suggested that SAA inhibition unexpectedly increased *CEACAM1* expression in neutrophils. Beyond neutrophils, TIM-3 blockade also reshaped the macrophage compartment, increasing macrophage abundance while suppressing NLRP3 inflammasome activity. This observation is particularly relevant given the enrichment of both neutrophils and macrophages in non-responders. Notably, macrophages exhibited the highest expression of HAVCR2 (TIM-3) across major cell types, providing a mechanistic basis for their direct responsiveness to TIM-3 inhibition. Together, these data support a unified model in which TIM-3/PD-1 co-blockade overcomes resistance by reinvigorating exhausted T cells while simultaneously reprogramming pathogenic myeloid inflammation.

Our study has certain limitations concerning data collection, analyses, and interpretation. First, although the cohort size ($n = 34$) is appropriate for scRNA-seq analysis, it remains modest for broad clinical generalization, particularly given inter-patient heterogeneity in RCC. Moreover, the acquisition of high-quality paired pre- and post-treatment samples was limited by biopsy feasibility and treatment-induced necrosis, restricting paired analysis. Larger independent prospective cohorts will be required to validate the clinical applicability of our findings. Second, our reliance on scRNA-seq data to infer cell type and state proportions may introduce measurement biases, particularly for certain cell populations, due to sampling and processing constraints. Nevertheless, our key findings regarding the enrichment of *SAA*$^+$ tumor cells and *VEGFA*$^+$ neutrophils and the depletion of $CD8^+$ T cells in non-responders were validated by mIHC, underscoring the reliability of these observations. Third, although ligand-receptor analysis suggested crosstalk between *SAA*$^+$ tumor cells and *VEGFA*$^+$ neutrophils, direct functional validation is still required. Future preclinical studies targeting SAA and CEACAM1 will be essential in clarifying the underlying mechanisms. Lastly, although our preclinical findings were consistent across multi-cohort datasets, spatial transcriptomics, mIHC, and in vivo models, clinical translation will require further validation, particularly given potential interspecies differences.

In summary, our study provides crucial mechanistic insights into treatment resistance and identifies clinically actionable strategies to improve outcomes in aRCC. Circulating SAA emerges as a promising predictive biomarker of therapeutic response. Mechanistically, SAA^+ tumor cells collaborate with $CEACAM1^+$ neutrophils to establish an immunosuppressive circuit that drives resistance. Targeting this pathway through SAA inhibition or blockade of CEACAM1/TIM-3 effectively reprograms the TME, restores antitumor immunity, and enhances the efficacy of combined ICI and TKI therapy.

Methods

Study design

This study was conducted in accordance with the Declaration of Helsinki and was approved by the Ethics Committee of the Chinese PLA General Hospital (PLAGH, Beijing, China; approval numbers: S2017-100 and S2019-349). All patients provided written informed consent for the collection and use of clinical data and specimens. Treatment response was assessed using Response Evaluation Criteria in Solid Tumors (RECIST) version 1.1 criteria. Patients whose best overall response was a partial response (PR) or complete response (CR) were classified as responders (R). The patients with stable disease (SD) or progressive disease (PD) were classified as non-responders (NR). Detailed clinicopathological information is summarized in Supplementary Datasets 1 and 2.

Animal experiments were performed in strict accordance with institutional guidelines and were approved by the Institutional Animal Care and Use Committee of the PLAGH. All mice were housed under specific pathogen-free conditions. The maximal permitted tumor burden was limited to no more than 10% of the animal' s body weight, in accordance with institutional regulations. Animals were monitored

https://doi.org/10.1038/s41467-026-70978-z

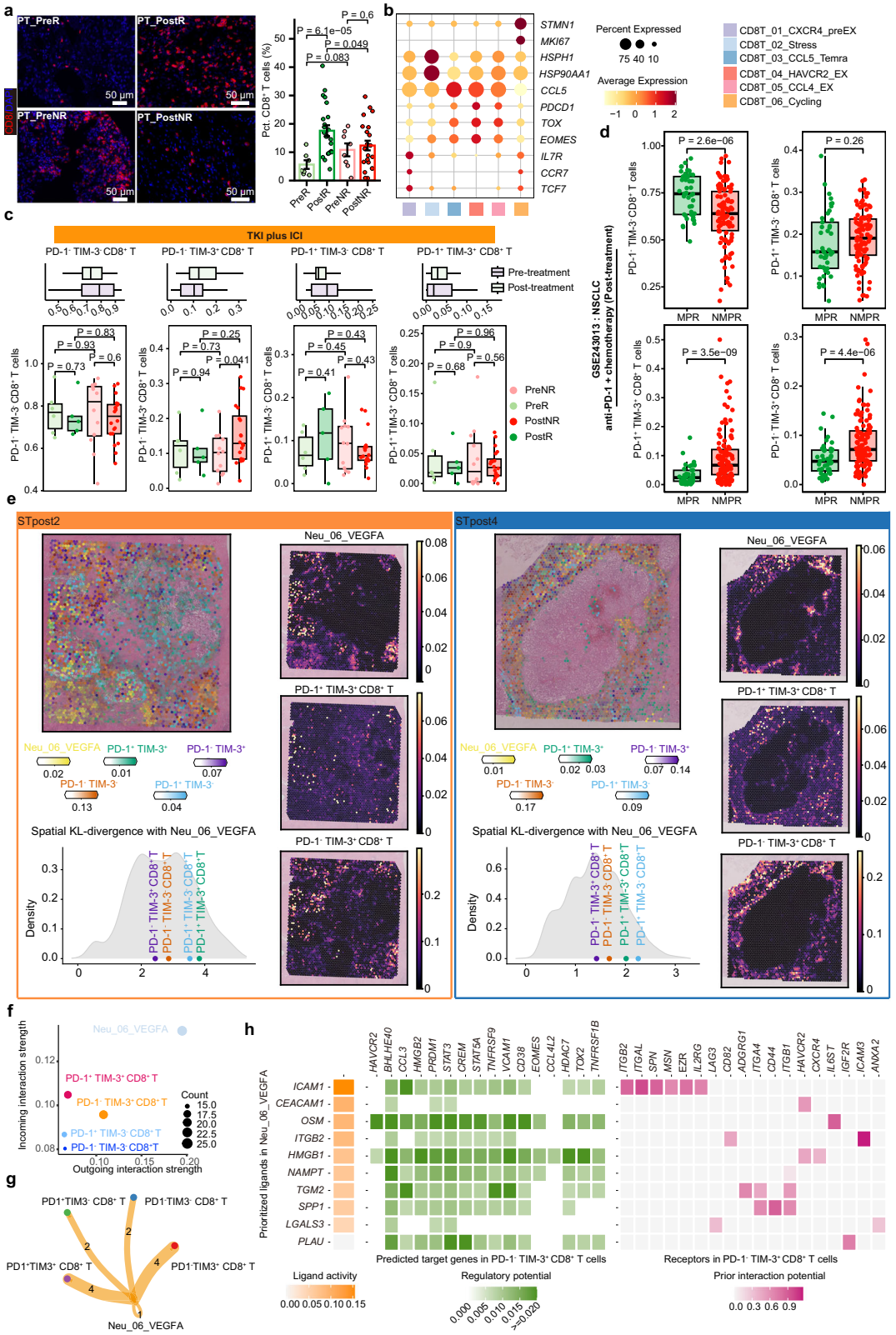

regularly for body weight, physical condition, and signs of distress. No animals exceeded the approved tumor burden or humane endpoint criteria during the study.

SeekOne® Single Cell 3′ Transcriptome (PLAGH cohort)

Fresh pre-treatment biopsies and post-treatment surgical specimens from the PLAGH cohort were processed using the SeekOne® Single Cell 3′ Transcriptome platform (SeekGene, China). Tissues were minced and enzymatically dissociated using the Multi-tissue Dissociation Kit (Miltenyi Biotec, #130-110-203), with DNase I adjusted according to sample viscosity. After red blood cell lysis (Miltenyi Biotec, #130-094-183), single-cell suspensions were filtered, counted, and assessed for viability using acridine orange/propidium iodide (AO/PI) staining on the Countstar® Rigel system. Where necessary, dead cells and debris

Fig. 5 | *VEGFA*$^+$ neutrophils interact with PD-1$^-$TIM-3$^+$ CD8$^+$ T cells to promote therapeutic resistance through CEACAM1–TIM-3 axis. a Representative mIHC images (left) and quantification (right) of CD8$^+$ T cell infiltration in PreNR ($n = 8$), PreR ($n = 7$), PostNR ($n = 23$), and PostR ($n = 23$) groups from the PLAGH cohort. Scale bars, 50 μm. *P* values were calculated using an unpaired two-sided *t*-test. Data are presented as mean ± SEM. **b** Dot plot showing representative exhaustion and activation marker expression across CD8$^+$ T cell subsets. Dot size represents the percentage of cells expressing the gene, and color indicates the scaled mean expression. **c** Quantification of four CD8$^+$ T cell subsets based on PD-1 and TIM-3 expression (PD-1$^-$TIM-3$^-$, PD-1$^-$TIM-3$^+$, PD-1$^+$TIM-3$^-$, and PD-1$^+$TIM-3$^+$) across treatment groups in the ICI plus TKI cohort (PreNR, $n = 12$; PreR, $n = 6$; PostNR, $n = 20$; PostR, $n = 5$). *P* values were calculated using an unpaired two-sided *t*-test. **d** Proportions of PD-1$^-$TIM-3$^+$, PD-1$^-$TIM-3$^-$, PD-1$^+$TIM-3$^-$, and PD-1$^+$TIM-3$^+$ CD8$^+$ T cells in NSCLC cohort (MPR, $n = 45$ *vs.* NMPR, $n = 112$; GSE243013). *P* values were calculated using an unpaired two-sided *t*-test. **e** Spatial mapping of cell types onto spatial transcriptomics (ST) slides from two post-treatment samples STpost2, and STpost4 using the spotiphy deconvolution method. Color intensity represents estimated relative abundance for all cell types (top left) and individual cell type (top right). The density plots display the KL divergence of the observed co-localization pattern relative to a null distribution derived from spatial permutation (bottom). **f** Interaction strength between Neu_06_VEGFA and different CD8$^+$ T subsets inferred by CellPhoneDB analysis in scRNA-seq data. Dot size represents predicted strength; axes indicate incoming/outgoing interaction scores. **g** Network diagram depicting predicted ligand–receptor interactions between Neu_06_VEGFA neutrophils and distinct CD8$^+$ T cell subtypes in the scRNA-seq dataset. Edge width reflects the predicted interaction strength. **h** NicheNet analysis showing predicted ligands expressed in Neu_06_VEGFA and their potential target genes and receptors in PD-1$^-$TIM-3$^+$ CD8$^+$ T cells. Color intensity indicates potential.

were removed (Miltenyi Biotec, #130-090-101/#130-109-398). Cells were resuspended in PBS containing 0.04% BSA at 1×10^6 cells/mL. Single-cell libraries were generated using either the SeekOne® MM (#K00301-0401) or DD (#K00202-0801) kit, following manufacturer protocols. Briefly, cells were loaded onto 170,000-well chips, followed by magnetic bead capture, lysis, reverse transcription, exonuclease digestion, second-strand synthesis, PCR amplification, and indexing. Libraries were purified, quantified (KAPA Biosystems, #KK4824), and sequenced using an Illumina NovaSeq 6000 system with PE150 reads.

Data processing and quality control for scRNA-seq (PLAGH cohort)

The raw Fastq sequencing data for each sample were processed using the SeekSoulTools software (version 1.2.2). During this processing, the data were aligned against the human hg38 reference genome, resulting in the generation of a raw gene expression count matrix. Subsequently, we utilized the CreateSeuratObject function in Seurat R package (version 4.1.0) to create a Seurat object with the default settings. Low-quality cells were then filtered out if they did not meet the following three criteria: (1) the total number of unique molecular identifiers (UMIs) per cell (library size) was greater than 300 and less than 30,000; (2) the number of detected genes per cell was above 100 and below 6,000; (3) the percentage of mitochondrial genes per cell was below 50. Notably, given the characteristically low transcript counts of neutrophils as documented in publications[16], we adjusted the acceptable range of the number of detected genes for neutrophils to be between 100 and 6000. Next, for each sample, we employed the scDblFinder R package (version 1.8.0) to identify and remove potential doublets. After the removal of low-quality cells and doublets, we employed regularized negative binomial regression using the SCTransform function in Seurat, to normalize the UMI counts, while regressing out the influence of the percentage of mitochondrial genes for each sample. Subsequently, we performed principal component analysis (PCA) for linear dimensionality reduction on the scaled data. The RunPCA function was used, and we retained 50 principal components. All the details regarding the Seurat analysis carried out in this study can be accessed through the online tutorial available at the following website: https://satijalab.org/seurat/articles/get_started.html.

Multiple scRNA-seq datasets integration and cell type annotation

A total of three scRNA-seq datasets associated with aRCC treatment were included in this study: the PLAGH scRNA-seq dataset (in-house data), the Chen et al.[7] scRNA-seq dataset (HRA004711), and the Msaouel et al.[8] scRNA-seq dataset (GSE264586). Subsequently, we employed the reciprocal principal components analysis (RPCA) pipeline in Seurat to integrate a total of 61 samples from these different studies. In detail, for each sample independently, we first performed normalization and identified 2000 features with high cell-to-cell variation as described above. Next, we selected features that were repeatedly variable across samples for integration using the SelectIntegrationFeatures function. Subsequently, we utilized the PrepSCTIntegration function to identify conserved features for integrating the datasets. Following this, we identified "anchors" between individual samples with the FindIntegrationAnchors function. These identified anchors were then input into the IntegrateData function, which generated a "batch-corrected" expression matrix of all cells. This enabled the integration and joint analysis of cells originating from different datasets. Finally, we utilized the top 50 principal components and set the resolution parameter to 0.8 as inputs for the FindNeighbors and FindClusters functions to cluster the cells. Non-linear dimensional reduction was carried out using the RunUMAP function with default settings. This process led to the identification of thirteen major cell clusters, which were further validated using known cell-lineage-specific marker genes listed in Supplementary Dataset 3.

Sub-clustering of major cell types

We further identified subpopulations within each major cell cluster by employing the same procedure as previously described[53]. Initially, we extracted cells corresponding to each major cell type from the integrated dataset (normal epithelial cells, stromal cells, T cells, B cells and plasma cells, monocytic cells, neutrophils and mast cells), respectively. Next, for each major cell type, we re-integrated the corresponding cells and conducted further sub-clustering, following the aforementioned methodology. During each sub-clustering step, we adjusted the resolution parameter in the Louvain algorithm within a range of 0.3–0.9 to optimize the clustering granularity. Following sub-clustering, we identified cluster-specific marker genes using Seurat's FindAllMarkers function and annotated the clusters based on well-established canonical cell type markers[16]. Additionally, we performed differential analysis using the MAST method, treating sample identity as a latent variable. Subcluster-specific marker genes are listed in Supplementary Datasets 4–10.

Identification and analysis of malignant cells

Single-cell copy number variants (CNVs) were detected using the CopyKAT R package (version 1.1.0) with the raw count matrix of scRNA-seq expression serving as the input[54]. Taking the counts of T cells, monocytes, macrophages, and dendritic cells (DCs) as references, the copycat function was used to infer CNVs in tumor cells (epithelial cells), with parameters set as ngene.chr = 5 and win.size = 25. Subsequently, each cell was categorized as either predicted diploid, aneuploid or not.defined.

Furthermore, we performed sub-clustering analysis for all epithelial cells[55]. We applied the FindAllMarkers function in Seurat to identify specific genes for each cell subset, which was conducted based on the MAST method[56], with sample identity treated as a latent variable to account for potential sample-specific variations.

https://doi.org/10.1038/s41467-026-70978-z

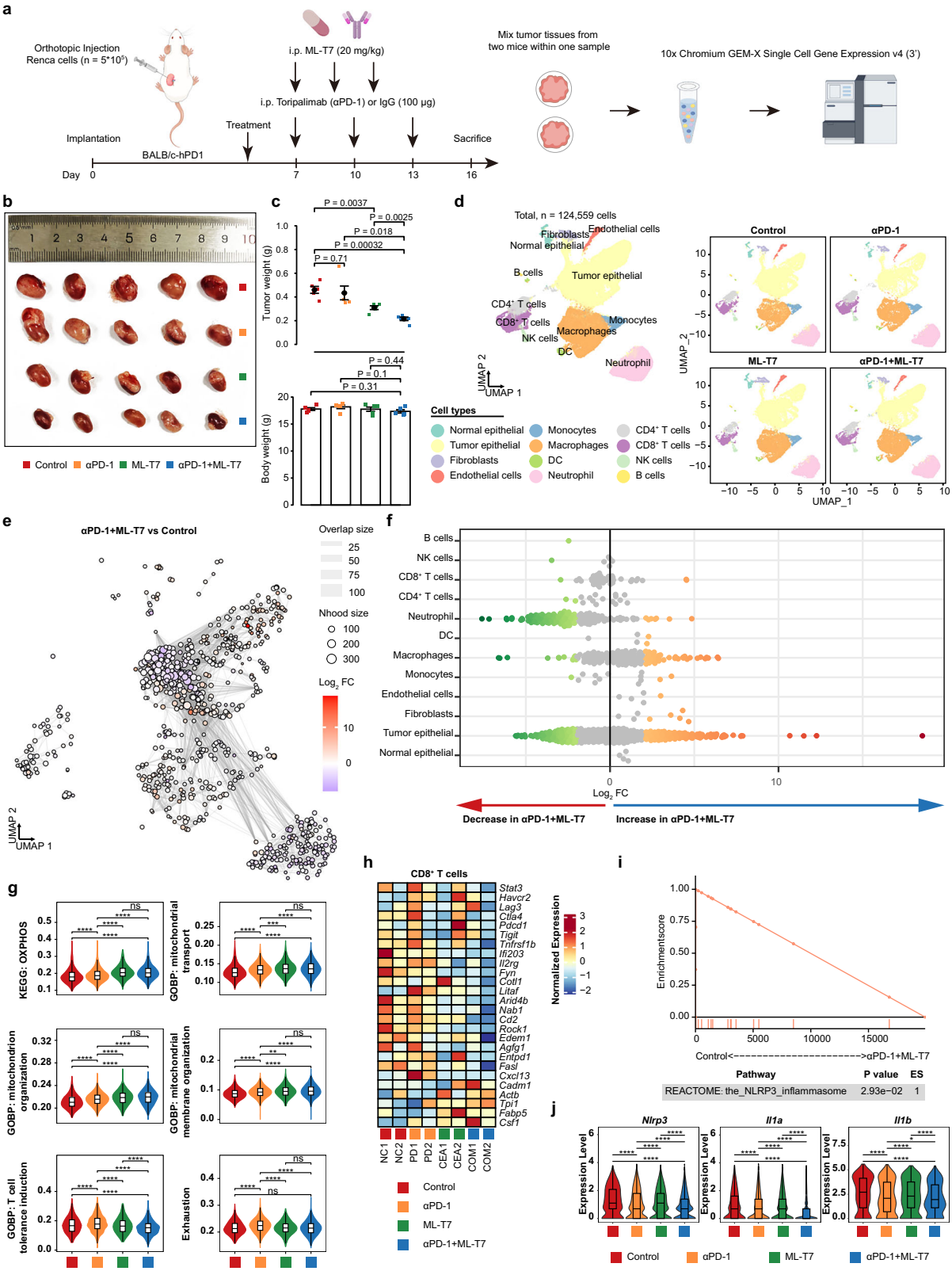

Additionally, we obtained DEGs between tumor and normal samples from bulk RNA-seq data of the TCGA-KIRC dataset using the limma R package (version 3.50.0). Subsequently, we extracted the top 3,000 signature genes from the TCGA dataset, comparing tumor and normal samples. Specifically, malignant signature genes were selected as the top 1500 highly expressed genes (adjusted $p < 0.01$) in tumor tissues, while non-malignant signature genes were chosen as the top 1500 highly expressed genes (adjusted $p < 0.01$) in normal tissues.

For diploid, aneuploid, or undefined cells within a single sample, further grouping based on cell subgroups (Epi0 to Epi7) generated new groups with distinct ploidy and transcriptional states, which were collectively referred to as "cell state". Next, we generated gene-by-cell state expression matrix by using the AverageExpression

Fig. 6 | CEACAM1–TIM-3 blockade alleviates anti–PD-1 resistance in RCC. **a** Schematic illustration of experimental workflow using a humanized PD-1 mouse model (BALB/c-hPD1, $n = 5$). **b** Representative images of orthotopically implanted tumors across treatment groups ($n = 5$). **c** Quantification of tumor weight (top) and body weight (bottom) in each group ($n = 5$). *P* values were calculated using an unpaired two-sided *t*-test. Data are presented as mean ± SEM. **d** UMAP plots showing clustering of 124,559 single cells into 12 major cell types across four treatment groups. **e** Differential abundance analysis by MiloR comparing Toripalimab + ML-T7 versus control groups. Nhood size corresponds to circle size, and overlap size corresponds to line thickness. The color scale indicates the log_2FC between Toripalimab + ML-T7 and control groups. **f** Beeswarm plot showing the enrichment (orange) or decrease (green) of neighborhoods in the Toripalimab + ML-T7 group for each indicated cell type calculated using MiloR. **g** Violin plots showing $CD8^+$ T cell pathway activity scores across treatment groups (Control, $n = 1031$; αPD-1, $n = 3071$; ML-T7, $n = 618$; αPD-1 + ML-T7, $n = 1544$), including oxidative phosphorylation (OXPHOS), mitochondria-related pathways, T cell tolerance induction and exhaustion. '*n*' represents the number of single cells that passed quality control and were included in the analysis. *P* values were calculated using an two-sided Wilcoxon rank-sum test. *P* values less than 0.01, 0.001, and 0.0001 were considered statistically significant, denoted by **, ***, and ****, respectively. **h** Heatmap showing expression of representative metabolic and exhaustion-associated genes in $CD8^+$ T cells across treatment groups, color indicates the normalized expression. **i** GSEA comparing macrophages from Toripalimab + ML-T7 *vs.* control, highlighting downregulation of the NLRP3 inflammasome pathway. Statistical analysis by an adaptive multi-level split Monte-Carlo scheme. **j** Violin plots showing expression of *Nlrp3*, *Il1a*, and *Il1b* in macrophages across groups (Control, $n = 4033$; αPD-1, $n = 4961$; ML-T7, $n = 7780$; αPD-1 + ML-T7, $n = 7465$). "*n*" represents the number of single cells that passed quality control and were included in the analysis. *P* values were calculated using an two-sided Wilcoxon rank-sum test. *P* values less than 0.05 and 0.0001 were considered statistically significant, denoted by * and ****.

function. To classify tumor cells, we took the log-transformed gene expression values of the malignant and non-malignant signature genes from the TCGA-KIRC dataset to construct a predictor by calculating the centroids of these selected features for both subtypes in the feature space.

Malignant and non-malignant cells were assigned to the nearest centroid based on the Pearson correlation coefficient. This analysis was carried out using the cancerclass R package (version 1.40.0). Cells expressing *PTPRC* were excluded from the analysis.

Non-negative matrix factorization (NMF)

We investigated the expression programs underlying intratumor heterogeneity within malignant cells derived from PreR, PreNR, PostR, and PostNR groups using NMF. Only patients with at least 100 malignant cells were included in the analysis to ensure robust results. Briefly, for each tumor sample, we initially normalized the expression counts using the SCTransform function in Seurat. During normalization, we regressed out the percentage of mitochondria genes as well as cell cycle effects, including S phase and G2/M phase signature scores. Subsequently, we extracted center-scaled data for the 2000 most highly variable genes (HVGs). Negative values in the expression matrix were replaced with zero to comply with the non-negativity requirement of NMF. We then used the nmf function in the NMF R package (version 0.25) to dissect the top 10 ranked co-expressed gene modules in each tumor sample. For each identified gene module, we selected the top 50 genes with the highest weights. These genes were used to define a specific intra-tumor expression program. In total, we identified 490 expression programs across 49 tumor samples. The pairwise Jaccard index for all programs was calculated as follows:

$$Jaccard\ index = \frac{programA \cap programB}{programA \cup programB} \quad (1)$$

where *programA* and *programB* denote two distinct intratumor expression programs.

Finally, only expression programs with a Jaccard index >0.1 were retained, resulting in 306 non-redundant expression programs. These programs were then grouped into metaprograms via hierarchical clustering with the "ward.D2" method. The Jaccard index served as the similarity metric for this clustering analysis. For each metaprogram, genes shared by at least five expression programs were defined as meta-signatures. This process resulted in the identification of nine metaprograms, including: cell cycle, neuronal-like, chemokine regulation, proximal tubule, EMT I and II, MHC-II, stress response, and an undefined metaprogram. The undefined metaprogram was excluded from further analysis. The gene signatures of the eight remaining metaprograms are listed in Supplementary Dataset 13.

Definition of predictive index and therapeutic index

To overcome the constraints imposed by limited sample sizes, we applied the Predictive Index (Pi) and the Therapeutic Index (Ti) to integrate scRNA-seq data with continuous measurements of tumor size changes. The Pi was designed to evaluate whether the baseline proportion of immune cell populations correlates with treatment-induced changes in tumor size. These tumor size changes were quantified as the relative differences in tumor dimensions between post-treatment and pre-treatment samples. Mathematically, the Pi is defined as follows:

$$Pi = \frac{-slope}{|slope|} \times R^2 \quad (2)$$

where the *slope* and R^2 values were derived from a linear regression model, denoted as lm(y1 ~ x1). This model was employed to estimate the correlation between the baseline cellular proportions (x1) of the respective immune cell clusters and the tumor size changes (y1) observed in patients undergoing different treatment regimens. A positive Pi indicates that a higher baseline level of the corresponding immune cell cluster is associated with a more favorable response to TKI and/or ICI therapy. Conversely, a negative Pi suggests that a higher baseline level of the relevant immune cell cluster is linked to a poorer response to TKI and/or ICI therapy.

The Ti, in contrast, was used to assess whether dynamic changes in immune cell proportions over the course of treatment correlate with tumor size alterations. Specifically, immune dynamics were calculated as the relative change in cell-type proportions between pre-treatment and post-treatment samples. The Ti is defined as follows:

$$Ti = \frac{-slope}{|slope|} \times R^2 \quad (3)$$

where the *slope* and R^2 values were derived from a linear regression model, denoted as lm(y2_x2). This model was employed to estimate the correlation between the changes in cellular proportions ($x2$) of the corresponding immune cell cluster and the alterations in tumor size ($y2$) observed in patients receiving different treatment regimens. A positive Ti indicates that an increased level of cellular proportion for the relevant immune cell cluster is associated with a more favorable clinical response. Conversely, a negative Ti suggests that an increased level of cellular proportion for this cell cluster is linked to a less favorable clinical response. Overall, the methodologies adopted in this study were analogous to those utilized in a previously published triple-negative breast cancer study[9].

Tissue enrichment analysis of clusters

To quantify the enrichment of cell types across distinct tissue groups—namely PreR, PostR, PreNR, and PostNR—we conducted a systematic comparison of the "Observed" and "Expected" cell counts within each cell cluster. This comparison was enabled by calculating the ratio of observed to expected cell counts ($R_{o/e}$), following the formula below[57]:

$$R_{o/e} = \frac{Observed}{Expected} \quad (4)$$

The expected number of cells for each cell type within a given tissue group was determined using a Chi-squared test based on overall cell distributions. A cell cluster was considered enriched in a specific tissue group if $R_{o/e} > 1$, indicating a higher-than-expected representation of that cluster in the group.

Pseudo-bulk differential expression analysis

DEGs between different conditions derived from scRNA-seq were identified using a pseudobulk analysis strategy. In brief, for each sample-cell type pairing, pseudobulk count data were generated using the AggregateExpression function from Seurat, applied to the raw count matrix. Subsequently, these pseudobulk count matrices were imported into the DESeq2 R package (version 1.40.2) to calculate DEGs. A negative binomial generalized linear model was used, without incorporating covariates. DEGs were computed for each PostNR group in comparison to the PostR. Only genes that were significantly differentially expressed, defined by a $P < 0.05$ and a $\log_2$ fold change ($\log_2$FC) > 1, were considered. This selection criterion focused solely on upregulated genes.

Gene set enrichment analysis (GSEA)

Overrepresentation analysis of gene sets was performed using the "fora" function within the fgsea R package (version 1.20.0).

The fgsea R package was used to assess differential enrichments of gene sets between two different groups of cell subsets. For the comparison of a specific cell type across two conditions, we utilized the FindMarkers function in Seurat to the $\log_2$FC values for all genes. These $\log_2$FC values served as the ranking metric for downstream GSEA.

The Hallmark[58], KEGG[59], Reactome[60], and Gene Ontology (GO) gene sets[61] were obtained from the msigdbr R package (version 7.4.1) and the Molecular Signatures Database (MSigDB) website (http://software.broadinstitute.org/gsea/msigdb). In addition to these well-established gene sets, we curated custom gene sets from previously published studies. Specifically, RCC-related meta-program signatures were obtained from Li et al.[27], a pan-cancer neutrophil signature from Wu et al.[14], and aPD-1 responder signature Sade- Feldman M et al.[62].

Gene signature identifying and scoring

We applied the FindAllMarkers function in Seurat to identify the specific genes for each cell subset. This analysis was conducted based on the MAST method[56], with sample identity incorporated as a latent variable to account for potential sample-specific effects. To select signature genes, we chose the top 50 cell-specific marker genes based on their average expression levels.

Based on the scRNA-seq data, we computed multiple gene signature scores. For each gene signature, individual cell scores were assigned using the AddModuleScore_UCell function from the UCell R package (version 1.3.1). The function was applied with its default settings. For bulk RNA-seq or pseudobulk data, we evaluated the signature score of a gene set in a sample based on the normalized gene expression. This was achieved using the single sample gene set enrichment analysis (ssGSEA)[63] method implemented in the GSVA R package (version 1.44.5).

For the correlation analysis, we employed the cor function from the stats R package (version 4.1.1). All correlation coefficients (Rho) and their corresponding *p*-values were determined through Pearson correlation analysis.

Trajectory analysis

Monocle2 (version 2.22.0) enabled us to elucidate the complex progression of neutrophils toward the ICI plus TKI resistant phenotype[64]. By employing the differentialGeneTest function, we identified genes with a $q < 0.05$. These genes were then used to order the cells in pseudotime analysis. Once the cell trajectories were established, we applied the Branched Expression Analysis Modeling (BEAM) approach to identify genes that exhibited differential expression between the trajectory branches[65]. For genes that showed significant branch-dependence (adjusted $P < 0.05$), we visualized their expression patterns across pseudotime using the plot_genes_branched_heatmap function.

We also analyzed the lineage developmental trajectory of neutrophils using the Monocle3 R package (version 1.0.0)[66]. The count matrix, which included gene expression profiles from neutrophils, along with the UMAP embeddings obtained during sub-clustering, were incorporated into a CellDataSet object. Subsequently, we partitioned the cells using the cluster_cells function. Based on this clustering, we inferred a trajectory graph using the learn_graph function. The pseudotime for each individual cell was then calculated by applying the order_cells function. Specifically, the neutrophil subtype with the highest *MMP9*$^+$ neutrophil signature was designated as the root state for pseudotime calculation. The trajectory analysis of CD8$^+$ T cells was conducted following the procedures described above.

RNA velocity analysis

To investigate the potential for cell transition among CD8$^+$ T cell subtypes, we integrated velocyto (version 0.17.15)[67] and Dynamo (version 1.4.0)[68] to calculate and visualize the ratio of spliced to unspliced transcripts in each CD8$^+$ T cell subtype. This approach enabled us to infer their respective maturation states. In detail, we initiated the process by generating Loom files for all samples from their corresponding BAM files. This step was carried out using velocyto with the GENCODE GRCh38 genome annotation file. Subsequently, we followed the standard workflow in Dynamo to compute RNA velocity values for each gene in every cell.

Cell-cell interactions analyses

The CellChat R package (version 1.6.1)[69], containing the ligand–receptor interaction databases for human, was used to establish the intercellular communication networks among different cell clusters. Initially, we used the CellChatDB.human function within CellChat to assess the primary signaling inputs and outputs across all cell clusters. For subsequent analyses, we selected receptors and ligands that were expressed in more than 10 cells within a candidate cell cluster. The interactions between distinct cell clusters via putative ligand–receptor pairs were visualized using the ggplot2 R package (version 3.5.1).

NicheNet analysis, facilitated by the nichenetr R package (version 1.1.1), was used to detect potential ligands originating from *SAA*$^+$ tumor cells that contribute to the distinctive phenotype displayed by Neu_06_VEGFA. We utilized the Seurat-based implementation of NicheNet for this analysis. A gene was considered as expressed if it had non-zero expression in at least 10% of the cells within a specific cell type. The calculation to determine the top ligand-receptor pairs was executed for each cell type using the nichenet_seuratobj_cluster_de function. In this function, *SAA*$^+$ tumor cells were designated as the sender, Neu_05_MMP9 as the receiver_reference, and Neu_06_VEGFA as the receiver_effected. Genes that were differentially expressed

between Neu_05_MMP9 and Neu_06_VEGFA (with a $\log_2$FC > 0.4 and an adjusted $P < 0.05$) were regarded as the gene set of interest.

Public single-cell RNAseq data analysis

We downloaded the raw UMI count matrices and associated cell annotations from scRNA-seq datasets derived from three patient cohorts: NSCLC patients treated with anti–PD-1 in combination with chemotherapy (GSE243013), HCC patients treated with anti–PD-1 in combination with lenvatinib (GSE235863), and CRC patients treated with anti–PD-1 (GSE236581). Subsequently, the raw UMI counts were normalized and filtered using Seurat, following the procedures described above.

The dataset (raw counts matrix) from Bi et al.[38], which is associated with RCC patients treated with anti–PD-1 in combination with TKIs, was downloaded from the Single Cell Portal (https://singlecell.broadinstitute.org/single_cell/study/SCP1288/tumor-and-immune-reprogramming-during-immunotherapy-in-advanced-renal-cell-carcinoma#study-summary). The dataset (raw counts matrix) from Krishna et al.[12], related to RCC patients treated with anti–PD-1 in combination with anti-CTLA-4, was downloaded from https://trace.ncbi.nlm.nih.gov/Traces/index.html?view=analysis&acc=SRZ190804. The dataset (raw counts matrix) from Hu et al.[70], which is associated with NSCLC patients treated with anti–PD-1 in combination with chemotherapy, was downloaded from the GEO portal (GSE207422). We utilized the raw counts matrix to create a Seurat object. This object was then normalized using Seurat's SCTransform function[71]. After that, it was integrated and re-clustered according to Seurat's RPCA, FindIntegrationAnchors, and IntegrateData methods following the description provided above.

To validate the transcriptomic states identified in our dataset, we performed label transfer of neutrophils using Seurat. We used the scRNA-seq dataset of neutrophils from our previously annotated dataset as the reference, and the scRNA-seq dataset of neutrophils from the Hu et al. dataset as the query. In brief, we computed transfer anchors between the reference and our query dataset using the FindTransferAnchors function. This function is based on shared gene expression and mutual nearest neighbors (MNNs) in a shared low-dimensional space. Next, we employed these anchors to assign cell type labels and project the reference dimensional reduction onto our dataset using the MapQuery function.

The dataset from Stone et al.[33] (GSE232696), related to the *Saa*$^{-/-}$ mouse model, was also included. Subsequently, it was imported into R using the CreateSeuratObject function in Seurat. In brief, the scRNA-seq data was normalized using the SCTransform function. After that, it was integrated and re-clustered according to Seurat's RPCA, FindIntegrationAnchors, and IntegrateData methods following the description provided above. These cell clusters were then annotated based on known cell-lineage-specific markers.

Spatial transcriptomic (ST)

Sample preparation and library construction. RNA was extracted from formalin-fixed, paraffin-embedded tumor (FFPE) tissue blocks using the RNeasy FFPE Kit (Qiagen, #73504), and RNA quality was assessed by calculating the DV200 value. Tissue sections passing quality control (DV200 > 30%) were used for ST analysis according to the Visium CytAssist Spatial Gene Expression protocol (10x Genomics, CG000495, CG000518, CG000520). Five-micrometer tissue sections were mounted on Visium-compatible glass slides and processed through dewaxing, staining, and cross-linking with a human whole-transcriptome probe set. After target–probe hybridization, the slides were processed on the Visium CytAssist instrument for permeabilization and RNase treatment. The hybridized probes were then ligated to spatially barcoded oligonucleotides. Library preparation was performed using the Visium CytAssist Spatial Gene Expression for FFPE Human Transcriptome Probe Kit (10x Genomics, #100044). The libraries were sequenced on an Illumina NovaSeq X Plus at Annoroad Gene Technology (Beijing, China).

Spatial transcriptomics data analysis. The raw sequencing reads from spatial ST underwent quality checking and were mapped to the human transcriptome reference GRCh38-2020-A using SpaceRanger (version 3.0.1). The gene-spot matrices, generated subsequent to ST data processing, were analyzed using the Seurat R package. We filtered out Visium spots with fewer than 200 total counts or 500 detected genes, as well as spots with >25% mitochondrial gene content. The filtered count matrices underwent normalization via the SCTransform function. Dimensionality reduction and clustering operations were carried out using the RunPCA, FindNeighbors, and FindClusters functions in Seurat. Specifically, these functions were applied at a resolution of 0.4, incorporating the first 30 principal components (PCs), with the aim of identifying spatial niches. The sample information is presented in Supplementary Dataset 1 and 2.

Celltype deconvolution and tumor core annotation. The Redeconve R package (version 1.1.0)[72] was employed to perform deconvolution of ST spots into distinct cell types by applying its deconvoluting function. Our scRNA-seq dataset was used as a reference, while the ST data functioned as the query dataset. Subsequently, the cell-type deconvolution data were added to the metadata of the Seurat object for downstream analysis.

The genome-wide copy numbers at the spot level were inferred from the transcriptomic data using the CopyKAT R package with the following specified parameters: "ngene.chr = 5, win.size = 25, KS.cut = 0.15, genome = hg20". After that, the identified diploid and aneuploid states were extracted from CopyKAT and integrated into the metadata of the Seurat object, enabling subsequent downstream analysis.

The activities of Hallmark gene sets specific to a spatial niche were quantified using the "ssGSEA" approach, leveraging the aggregated gene expression profile. Subsequently, spatial niches within the tissue section were grouped through agglomerative clustering employing the complete linkage method, which relied on the Euclidean distance derived from the gene-set activities.

A spatial niche was classified as a "tumor core" if it met all of the following conditions: (1) cell type deconvolution by Redeconve estimated a tumor cell proportion greater than 25%; (2) CopyKAT estimated an aneuploid *vs.* diploid probability exceeding 20%; and (3) elevated pathway activity in DNA repair and MYC TARGETS V1/V2 signatures. In addition, all "tumor core" regions were pathologically confirmed as RCC by a board-certified pathologist.

Cell type co-localization analysis. The spatial co-localization index between cell types of interest was computed using a previously described analytical pipeline[73]. Cell type co-localization analysis was performed as previously described with minor adjustments[73,74]. To assess the spatial co-localization between VEGFA$^+$ neutrophils and CD8$^+$ T cell subsets, we leveraged cell type deconvolution results generated by the spotiphy algorithm (version 0.3.1)[75] from ST slides. For each cell type of interest, we computed a weighted two-dimensional kernel density estimate across the tissue section using the wkde2d function in the Nebulosa R package (version 1.16.0), with spot-level deconvolved proportions as weights. This yielded continuous spatial density maps reflecting the local enrichment of each cell population. We then quantified the similarity between the spatial distributions of any two cell types using the Kullback–Leibler (KL) divergence, calculated via the KL function in the philentropy R package. Lower KL divergence values indicate greater spatial overlap. Subsequently, we generated a null distribution of KL divergence values by permuting cell type assignments across ST spots. Specifically, we randomly shuffled the deconvolution matrix 1,000 times while

preserving the 80% of spots and cell type proportions per spot. For each permutation, we recomputed the density maps and KL divergence for the same cell type pair.

Bulk RNA-seq and survival analysis. Survival analyses were conducted across multiple patient cohorts that underwent bulk RNA-seq and were subjected to diverse treatments with varying endpoints. These cohorts included the TCGA-KIRC cohort, IMmotion150[76], the JAVELIN Renal 101 trial[77], Checkmate[78], the study by Zhang et al.[79], IMvigor210[80] and the study by Liu et al.[81]. Subsequently, the signature scores and the expression levels of SAA genes (calculated as the mean value of *SAA1* and *SAA2*) were dichotomized according to the optimal cut-off point determined by the surv_cutpoint function from the survminer R package (version 0.5.0). KM survival curves were generated to visualize survival differences, and two-sided log-rank tests were used to determine statistical significance. A $P < 0.05$ was considered statistically significant.

Furthermore, univariate Cox proportional hazards regression analysis was carried out using the coxph function from the survival R package (version 3.7.0), and the results were visualized in forest plots using the forestmodel R package (version 0.6.2).

Antibodies, reagents, key commercial kit and software. Detailed information on the antibodies, key reagents, cell lines, animal strains, software and algorithms used in this study is provided in Supplementary Dataset 19.

Isolation and culture of neutrophils. Peripheral blood samples were obtained from treatment-naïve RCC patients. Neutrophils were isolated using magnetic bead–based separation according to the manufacturer's instructions (CD15 MicroBeads, human; Miltenyi Biotec; #130-046-601), yielding >99% $CD15^+$ purity as assessed by flow cytometry. Purified neutrophils were cultured in complete RPMI-1640 medium supplemented with 10% FBS and stimulated with recombinant human SAA1 protein (Absin, #abs05051) for 12 h. After stimulation, neutrophils were collected by centrifugation and subsequently used for flow cytometric analysis and RNA extraction.

Flow cytometry. After stimulation, neutrophils were harvested, washed with PBS, and stained for surface markers. Cells were incubated with PE anti-human CD15 (SSEA-1; BioLegend; #301906) and Alexa Fluor® 647 anti-human CD66a/c/e (BioLegend, #342318) according to the manufacturer's instructions. After staining, cells were washed and resuspended in staining buffer for acquisition. Data were acquired using an Attune NxT Flow Cytometer (Thermo Fisher Scientific) and analyzed with FlowJo software (v10.8.1).

Quantitative real-time PCR (qRT-PCR). Total RNA was extracted from neutrophils using the FastPure Cell/Tissue Total RNA Isolation Kit V2 (Vazyme, #RC112-01). First-strand cDNA was synthesized using the HiScript IV RT SuperMix (Vazyme, #R423-01) according to the manufacturer's instructions. Quantitative real-time PCR was performed using SYBR FAST PCR Master Mix (Vazyme, #Q712-02) on a CFX96 Touch Real-Time PCR Detection System (Bio-Rad). Relative mRNA expression was calculated using the ΔCt method, with *PPIA* as the internal control. PCR primers were designed and synthesized by Biomed (China), and sequences for *PPIA* and *CEACAM1* are listed in Supplementary Dataset 19.

SAA blockade in vivo. For the orthotopic RCC model, Renca-Luc cells (HyCyte, #TCM-C784L; 1×10^6 cells in 50 µL Matrigel; LABLEAD, #MG6248) were implanted into the right kidney of 5-week-old male BALB/c mice (GemPharmatech, #N000020). Seven days post-implantation, mice were randomized into four groups ($n = 5$ per group):

(1) Vehicle control: i.p. injection of IgG (#A2123, Selleck; 100 µg/mouse, every 3 days, total 3 doses) and daily i.g. administration of 1% CMC-Na (Selleck, #S6703).
(2) SAA blockade: i.p. injection of anti-SAA1/2 antibody (R&D Systems, #AF2948; 5 µg/mouse, twice weekly, total 2 doses) plus daily i.g. administration of 1% CMC-Na.
(3) Combination group: i.p. injection of anti–PD-1 antibody (Selleck, #A2122; 100 µg/mouse, every 3 days, total 3 doses) plus Axitinib (Selleck, #S1005; 30 mg/kg/day, i.g., total 7 doses).
(4) Triple combination therapy: anti-SAA1/2 antibody, anti–PD-1 antibody, and Axitinib were administered following the same dosing schedules as in groups (2) and (3).

Mice were housed under a 12 h light/12 h dark cycle at a controlled temperature (22–25 °C) and humidity (50–60%). On day 16 post-implantation, mice were euthanized via CO_2 asphyxiation. Body weight and kidney weight were measured and recorded.

CEACAM1–TIM-3 blockade in vivo. In the CEACAM1–TIM-3 blockade model, Renca-Luc cells (5×10^5 suspended in 50 µl of Matrigel; LABLEAD, #MG6248) were orthotopically injected into the right kidney of 5-week-old male BALB/c-hPD-1 humanized mice (#T002726, GemPharmatech, China). After 7 days, mice were randomly allocated to four groups ($n = 5$ per group):

(1) Vehicle control: i.p. injection of IgG (Selleck, #A2052; 100 µg/mouse, every 3 days, total 3 doses).
(2) CEACAM1–TIM-3 blockade: i.p. administration of ML-T7 (MCE, #HY-163028; 20 mg/kg, every 2 days, total 3 doses).
(3) PD-1 blockade: i.p. injection of Toripalimab (TopAlliance, #JS001; 100 µg/mouse, every 3 days, total 3 doses).
(4) Combination therapy: both ML-T7 and Toripalimab were administered using the same regimens as in groups (2) and (3).

Mice were housed under a 12 h light/12 h dark cycle at a controlled temperature (22–25 °C) and humidity (50–60%). On day 16 post-implantation, mice were euthanized via CO2 asphyxiation. Body weight and kidney weight were measured and recorded.

Mouse single-cell preparation and 10x Genomics GEM-X sequencing. Tumor specimens were harvested from mice treated in the in vivo CEACAM1–TIM-3 blockade experiment. For each sample, tumors from two mice were pooled. Tumor tissues were enzymatically digested to obtain single-cell suspensions, which were sequentially filtered through 70-µm and 30-µm strainers (Miltenyi Biotec, #130-098-458 and #130-098-462). Red blood cells were lysed using red blood cell lysis (Miltenyi Biotec, #130-094-183). Cell viability was assessed using Countstar® Rigel, and Dead Cell Removal Kit (Miltenyi Biotec, #130-090-101) was used when necessary to remove dead cells. Cells were resuspended in PBS with 0.04% BSA at a final concentration of 700–1200 cells/µL.

Single-cell libraries were prepared using the Chromium Single Cell 3' Reagent Kit v4 (10x Genomics, #1000691) and Chromium Chip v4 (10x Genomics, #1000690) following the manufacturer's protocol provided by Novogene. RNA was barcoded on the Chromium X system. Subsequent steps, including reverse transcription, cDNA amplification, and library construction, were performed using the Chromium Library Construction Kit v4 (10x Genomics, #1000694). Final libraries were sequenced on an Illumina NovaSeq X Plus platform (PE150) at Novogene (Beijing).

Mouse single cell RNAseq analysis. Sc-RNAseq data were analyzed using our previously described bioinformatics pipeline, as detailed in ref. 82, with minor modifications tailored to this study. Briefly, data pre-processing and quality control were carried out separately for each library. Raw sequencing reads were pre-processed using cellranger

(version 8.0.1). First, raw bcl files were de-multiplexed with mkfastq, and then gene expression matrices were generated using cellranger "count" with the mouse GRCm39-2024-A reference genome. Low-quality cells were excluded if they did not meet all the following criteria: number of expressed genes (nFeature_RNA) > 100, <6000, and percentage of mitochondrial gene reads <25%. Doublets were removed using the scDblFinder R package with default settings (dbr = NULL; for 10x data, it is generally safe to leave the dbr parameter empty, and it will be automatically estimated). After filtering, 124,559 cells remained, with a median of 2187 genes detected per cell.

The cleaned datasets were then normalized using Seurat with SCTransform, following a Gamma-Poisson Generalized Linear Model. The data were scaled while regressing out the cell cycle scores and the percentage of expressed mitochondrial genes. To identify inter-sample anchors for sample integration, the FindIntegrationAnchors function was employed, using the top 3000 highly variable genes identified by the SelectIntegrationFeatures function across all samples. Subsequently, the IntegrateData function was used to generate a combined and batch-corrected expression matrix. PCA was performed using RunPCA with the top 50 principal PCs. Dimensionality reduction was carried out using RunUMAP with the top 50 dimensions. Nearest-neighbor analysis was conducted using FindNeighbors with the top 50 dimensions and a k.param value set to 50. Clustering was performed using FindClusters with a resolution of 0.6 to obtain an initial clustering result. Globally distinguishing marker genes for each cell cluster were identified using Seurat's FindAllMarkers function with the MAST method (Supplementary Dataset 18). Cell clusters were then preliminarily classified by manually inspecting marker genes. For more precise cell type classification, we followed the "sub-clustering of major cell types" step described above.

Enzyme-Linked Immunosorbent Assay (ELISA) assay. SAA levels in pretreatment plasma samples from patients were quantified using a Human SAA ELISA kit (Jonlnbio, #JL10489) following the manufacturer's protocol. The assay was performed in a sandwich ELISA format. Briefly, samples and standards were added to 96-well plates pre-coated with a capture antibody specific for human SAA. After incubation and washing, a biotin-conjugated detection antibody was added, followed by streptavidin–HRP. Color development was achieved using TMB substrate, and the reaction was stopped with an acidic stop solution. Absorbance was measured at 450 nm using a microplate reader, and SAA concentrations were calculated from a standard curve.

Multiplex immunohistochemistry (mIHC) and analysis. FFPE tissues were sectioned at 5 µm, deparaffinized in xylene and rehydrated through a graded ethanol series then washed with distilled water. Antigen retrieval was performed by microwaving in boiling EDTA buffer for 15 min. Blocking was carried out using Antibody Diluent/Block (Alpha X Bio). mIHC was performed using a 6-plex, 7-color staining panel. The following primary antibodies were used and incubated for 1 h at 37 °C:

Panel 1: CD66b (Abcam, #ab197678, 1:100), SAA (Abcam, #ab207445, 1:1000), pan-CK (ZSGB-BIO, #ZM0069, 1:200), and CD8 (ZSGB-BIO, #ZA0508, 1:100).

Panel 2: VEGFA (Proteintech, #66828-1-Ig, 1:1000), CD66a (ABclonal, #A26413PM, 1:8000), and CD66b (Abcam, #ab197678, 1:100).

Panel 3: VEGFA (ABclonal, #A17877, 1:2000), CD66a (ABclonal, #A26413PM, 1:8000), Ly6G (Servicebio, #GB11229, 1:600), and CD8 (Abcam, #ab21734, 1:2000).

Slides were then incubated with Alpha X Polymer HRP Ms+Rb (Alpha X Bio) for 10 min at 37 °C and developed using the Alpha X 7-Color IHC Kit (Alpha X Bio, #AXT37100041), with fluorophores assigned to each target antibody. Between staining cycles, antibody stripping was achieved by heat-mediated epitope retrieval. Nuclei were counterstained with DAPI. Whole-slide images were acquired using Axioscan 7 (ZEISS, v3.3) and analyzed using HALO software (Indica Labs, v3.6).

Quantification and statistical analyses. For all experiments, unless otherwise noted in the figure legends, the value of "*n*" denotes biologically independent samples. This includes independent experiments for in vitro assays, individual mice for animal studies, and individual patients for clinical analyses. Statistical analyses were conducted using R (version 4.1.1) and Python (version 3.8.12) to process sequencing data and analyze clinical variables. The repertoire of statistical analyses utilized in this study included Wilcoxon rank-sum test, Student's *t* test, Chi-square test, and the *P* values derived from GSEA enrichment. Log-rank tests were conducted to assess differences in survival outcomes. In the context of CellChat analysis, *P* values were computed via a one-sided permutation test to evaluate the significance of cell-cell communication patterns. The statistical tools and threshold for each analysis are explicitly described with the Results or detailed in the Figure Legends or "Methods" sections. $P < 0.05$ was considered statistically significant. In terms of statistical significance, multiple levels were defined: *p* values less than 0.05, 0.01, 0.001, and 0.0001 were considered statistically significant, denoted by *, **, ***, and ****, respectively. In all box plots, the center line in the boxplots indicates the median, the lower and upper hinges correspond to the first and third quartiles, and the whiskers extend at most 1.5 times the interquartile range past the upper and lower quartiles. In all bar graphs and dot plots, data are presented as mean ± standard error of the mean (SEM).

Reporting summary

Further information on research design is available in the Nature Portfolio Reporting Summary linked to this article.

Data availability

Source Data are provided with this paper. Additional data supporting the findings of this study are available from the corresponding author, Baojun Wang (baojun40009@126.com). The raw single-cell RNA-seq data generated in this study has been deposited in the Genome Sequence Archive (GSA) human database within the National Genomics Data Center (NGDC), under accession code HRA006643. The raw scRNA-seq count data from Renca humanized mouse models used in this study are available in the OMIX within the NGDC under accession code OMIX011087. The bulk RNA-seq data of the PLAGH cohort used in this study are available in the GSA under accession code HRA005878[73] (https://ngdc.cncb.ac.cn/gsa-human/browse/HRA005878).

The expression matrix and clinical data of TCGA-KIRC[83] was obtained from the website https://portal.gdc.cancer.gov/ (Project: TCGA-KIRC). The datasets from JAVELIN Renal 101 trial[77] and Checkmate[78], and Zhang et al.[79] were retrieved from the supplementary material of the original publications. The IMmotion 150[76] data was sourced from the European Genome-Phenome Archive (EGA) database (https://ega-archive.org/studies/EGAS00001002928), following approval from the Data Access Committee. Processed gene expression data from a urothelial carcinoma (UC) cohort (EGAS00001002556; https://ega-archive.org/studies/EGAS00001002556) that received atezolizumab treatment was obtained through the IMvigor210CoreBiologies R package[80]. Processed RNA-seq data in transcripts per million (TPM) matrix from melanoma patients treated with anti–PD-1 were acquired from a large melanoma genome sequencing project (https://www.ncbi.nlm.nih.gov/projects/gap/cgi-bin/study.cgi?study_id=phs000452.v3.p1)[81]. Processed RNA-seq data (TPM) from HCC patients treated with anti–PD-1 plus lenvatinib are available in the Gene Expression Omnibus (GEO) under accession number GSE235863[84]. Raw RNA-seq count data from the A-498 and 786-O RCC cell lines were downloaded from the GEO portal (GSE216494, https://www.ncbi.nlm.nih.gov/geo/query/acc.cgi?acc=GSE216494)[85].

The scRNA-seq data from patients with advanced RCC treated with sitravatinib in combination with nivolumab plus ipilimumab are available in GEO under accession number GSE264586[8]. The scRNA-seq data related to neoadjuvant TKI therapy in aRCC are available in the GSA under accession code HRA004711[7]. The scRNA-seq data for NSCLC (GSE243013[86], https://www.ncbi.nlm.nih.gov/geo/query/acc.cgi?acc=GSE243013; GSE207422[70], https://www.ncbi.nlm.nih.gov/geo/query/acc.cgi?acc=GSE207422), HCC (GSE235863[84], https://www.ncbi.nlm.nih.gov/geo/query/acc.cgi?acc=GSE235863), and CRC (GSE236581[87], https://www.ncbi.nlm.nih.gov/geo/query/acc.cgi?acc=GSE236581), which were used in this study, were downloaded from the GEO portal. The scRNA-seq data for RCC were obtained from two sources: the Single Cell Portal: (https://singlecell.broadinstitute.org/single_cell/study/SCP1288/tumor-and-immune-reprogramming-during-immunotherapy-in-advanced-renal-cell-carcinoma#study-summary)[38] and https://trace.ncbi.nlm.nih.gov/Traces/sra/sra.cgi?analysis=SRZ190804[12]. The scRNA-seq data from the Saa$^{-/-}$ mouse model are available in GEO under accession number GSE232696[33] (https://www.ncbi.nlm.nih.gov/geo/query/acc.cgi?acc=GSE232696).

Code availability

The code used in this study is available on GitHub (https://github.com/zhang-qi-max/PLAGHNeo) and has been archived in Zenodo (https://doi.org/10.5281/zenodo.18500615).

References

1. Choueiri, T. K. & Motzer, R. J. Systemic therapy for metastatic renal-cell carcinoma. *N. Engl. J. Med* **376**, 354–366 (2017).
2. Barragan-Carrillo, R. et al. First and second-line treatments in metastatic renal cell carcinoma. *Eur. Urol.* **87**, 143–154 (2025).
3. Siegel, R. L., Miller, K. D. & Jemal, A. Cancer statistics, 2017. *CA Cancer J. Clin.* **67**, 7–30 (2017).
4. Sharma, R. et al. Determinants of resistance to VEGF-TKI and immune checkpoint inhibitors in metastatic renal cell carcinoma. *J. Exp. Clin. Cancer Res* **40**, 186 (2021).
5. Gu, L. et al. Neoadjuvant toripalimab plus axitinib for clear cell renal cell carcinoma with inferior vena cava tumor thrombus: NEOTAX, a phase 2 study. *Signal Transduct. Target Ther.* **9**, 264 (2024).
6. McKinnon, M. B., Rini, B. I. & Haake, S. M. Biomarker-informed care for patients with renal cell carcinoma. *Nat. Cancer* **6**, 573–583 (2025).
7. Chen, W. J. et al. Preoperative neoadjuvant targeted therapy remodels intra-tumoral heterogeneity of clear-cell renal cell carcinoma and ferroptosis inhibition induces resistance progression. *Cancer Lett.* **593**, 216963 (2024).
8. Msaouel, P. et al. Sitravatinib in combination with nivolumab plus ipilimumab in patients with advanced clear cell renal cell carcinoma: a phase 1 trial. *Nat. Commun.* **16**, 578 (2025).
9. Zhang, Y. et al. Single-cell analyses reveal key immune cell subsets associated with response to PD-L1 blockade in triple-negative breast cancer. *Cancer Cell* **39**, 1578–1593 e1578 (2021).
10. Teillaud, J. L., Houel, A., Panouillot, M., Riffard, C. & Dieu-Nosjean, M. C. Tertiary lymphoid structures in anticancer immunity. *Nat. Rev. Cancer* **24**, 629–646 (2024).
11. Jammihal, T. et al. Immunogenomic determinants of exceptional response to immune checkpoint inhibition in renal cell carcinoma. *Nat. Cancer* **6**, 372–384 (2025).
12. Krishna, C. et al. Single-cell sequencing links multiregional immune landscapes and tissue-resident T cells in ccRCC to tumor topology and therapy efficacy. *Cancer Cell* **39**, 662–677 e666 (2021).
13. Li, K. et al. Multi-omic analyses of changes in the tumor microenvironment of pancreatic adenocarcinoma following neoadjuvant treatment with anti-PD-1 therapy. *Cancer Cell* **40**, 1374–1391 e1377 (2022).
14. Wu, Y. et al. Neutrophil profiling illuminates anti-tumor antigen-presenting potency. *Cell* **187**, 1422–1439 e1424 (2024).
15. Meng, Y. et al. Immunosuppressive CD10(+)ALPL(+) neutrophils promote resistance to anti-PD-1 therapy in HCC by mediating irreversible exhaustion of T cells. *J. Hepatol.* **79**, 1435–1449 (2023).
16. Xue, R. et al. Liver tumour immune microenvironment subtypes and neutrophil heterogeneity. *Nature* **612**, 141–147 (2022).
17. Chen, J. et al. CREB1-driven CXCR4(hi) neutrophils promote skin inflammation in mouse models and human patients. *Nat. Commun.* **14**, 5894 (2023).
18. Sharma, P. et al. Immune checkpoint therapy-current perspectives and future directions. *Cell* **186**, 1652–1669 (2023).
19. Zhang, N. et al. Multifaceted roles of Galectins: from carbohydrate binding to targeted cancer therapy. *Biomark. Res* **13**, 49 (2025).
20. Kammerer, R. et al. The tumour suppressor gene CEACAM1 is completely but reversibly downregulated in renal cell carcinoma. *J. Pathol.* **204**, 258–267 (2004).
21. Skubitz, K. M. The role of CEACAMs in neutrophil function. *Eur. J. Clin. Invest.* **54**, (Suppl 2), e14349 (2024).
22. Chen, C. et al. Soluble Tim-3 serves as a tumor prognostic marker and therapeutic target for CD8(+) T cell exhaustion and anti-PD-1 resistance. *Cell Rep. Med* **5**, 101686 (2024).
23. Huang, Y. H. et al. CEACAM1 regulates TIM-3-mediated tolerance and exhaustion. *Nature* **517**, 386–390 (2015).
24. Liu, H., Zhao, H., Zhou, M., Zhao, X. & Lu, Y. Neutrophils in cancer drug resistance: roles and therapeutic opportunities. *Cancer Lett.* **611**, 217417 (2024).
25. Li, Q. et al. Microbiome dysbiosis, neutrophil recruitment and mesenchymal transition of mesothelial cells promotes peritoneal metastasis of colorectal cancer. *Nat. Cancer* **6**, 493–510 (2025).
26. Cai, Y. et al. Inhibition of NR2F2 restores hormone therapy response to endocrine refractory breast cancers. *Sci. Transl. Med.* **17**, eadk7786 (2025).
27. Li, R. et al. Mapping single-cell transcriptomes in the intra-tumoral and associated territories of kidney cancer. *Cancer Cell* **40**, 1583–1599 e1510 (2022).
28. Urieli-Shoval, S., Linke, R. P. & Matzner, Y. Expression and function of serum amyloid A, a major acute-phase protein, in normal and disease states. *Curr. Opin. Hematol.* **7**, 64–69 (2000).
29. Alchahin, A. M. et al. A transcriptional metastatic signature predicts survival in clear cell renal cell carcinoma. *Nat. Commun.* **13**, 5747 (2022).
30. Xu, Z. et al. SAA1 has potential as a prognostic biomarker correlated with cell proliferation, migration, and an indicator for immune infiltration of tumor microenvironment in clear cell renal cell carcinoma. *Int. J. Mol. Sci.* **24**, 7505 (2023).
31. Wei, H. et al. MMPs-related risk model identification and SAA1 promotes clear cell renal cell carcinoma migration via ERK-AP1-MMPs axis. *Sci. Rep.* **14**, 9411 (2024).
32. He, M. et al. Serum amyloid A promotes glycolysis of neutrophils during PD-1 blockade resistance in hepatocellular carcinoma. *Nat. Commun.* **15**, 1754 (2024).
33. Stone, M. L. et al. Hepatocytes coordinate immune evasion in cancer via release of serum amyloid A proteins. *Nat. Immunol.* **25**, 755–763 (2024).
34. Galluzzi, L., Smith, K. N., Liston, A. & Garg, A. D. The diversity of CD8(+) T cell dysfunction in cancer and viral infection. *Nat. Rev. Immunol.* **25**, 662–679 (2025).
35. Waibl Polania, J. et al. Antigen presentation by tumor-associated macrophages drives T cells from a progenitor exhaustion state to terminal exhaustion. *Immunity* **58**, 232–246 e236 (2025).
36. Beltra, J. C. et al. Developmental relationships of four exhausted CD8(+) T cell subsets reveals underlying transcriptional and epigenetic landscape control mechanisms. *Immunity* **52**, 825–841 e828 (2020).

37. Miller, B. C. et al. Subsets of exhausted CD8(+) T cells differentially mediate tumor control and respond to checkpoint blockade. *Nat. Immunol.* **20**, 326–336 (2019).
38. Bi, K. et al. Tumor and immune reprogramming during immunotherapy in advanced renal cell carcinoma. *Cancer Cell* **39**, 649–661 e645 (2021).
39. Romero, D. Immunotherapy: PD-1 says goodbye, TIM-3 says hello. *Nat. Rev. Clin. Oncol.* **13**, 202–203 (2016).
40. Zhu, B. et al. Spatial and multiomics analysis of human and mouse lung adenocarcinoma precursors reveals TIM-3 as a putative target for precancer interception. *Cancer Cell* **43**, 1125–1140 e1110 (2025).
41. Zhao, L., Li, T., Zhou, Y., Wang, P. & Luo, L. Monoclonal antibody targeting CEACAM1 enhanced the response to anti-PD1 immunotherapy in non-small cell lung cancer. *Int Immunopharmacol.* **143**, 113395 (2024).
42. Zhu, Y. et al. Abstract 537: Preclinical PD-1 resistance models: crucial tools for unveiling PD-1 resistance mechanisms and advancing novel treatment strategies. *Cancer Res.* **84**, 537–537 (2024).
43. Ma, S. et al. Identification of a small-molecule Tim-3 inhibitor to potentiate T cell-mediated antitumor immunotherapy in preclinical mouse models. *Sci. Transl. Med* **15**, eadg6752 (2023).
44. Zhai, X. et al. Mitochondrial C1qbp promotes differentiation of effector CD8(+) T cells via metabolic-epigenetic reprogramming. *Sci. Adv.* **7**, eabk0490 (2021).
45. Sharma, B. R. & Kanneganti, T. D. NLRP3 inflammasome in cancer and metabolic diseases. *Nat. Immunol.* **22**, 550–559 (2021).
46. He, L. N. et al. Baseline and early changes in circulating Serum Amyloid A (SAA) predict survival outcomes in advanced non-small cell lung cancer patients treated with Anti-PD-1/PD-L1 monotherapy. *Lung Cancer* **158**, 1–8 (2021).
47. De Santo, C. et al. Invariant NKT cells modulate the suppressive activity of IL-10-secreting neutrophils differentiated with serum amyloid A. *Nat. Immunol.* **11**, 1039–1046 (2010).
48. Jin, J. et al. Sunitinib resistance in renal cell carcinoma: from molecular mechanisms to predictive biomarkers. *Drug Resist Updat* **67**, 100929 (2023).
49. Kim, W. M., Huang, Y. H., Gandhi, A. & Blumberg, R. S. CEACAM1 structure and function in immunity and its therapeutic implications. *Semin Immunol.* **42**, 101296 (2019).
50. Li, H. et al. Distinct CD8(+) T cell dynamics associate with response to neoadjuvant cancer immunotherapies. *Cancer Cell* **43**, 757–775 e758 (2025).
51. Dupuis, M. L. et al. The human antibody fragment DIATHIS1 specific for CEACAM1 enhances natural killer cell cytotoxicity against melanoma cell lines in vitro. *J. Immunother.* **38**, 357–370 (2015).
52. Macarulla, T. et al. Abstract 7141: final analysis of the randomized Phase 2 cohort of CM24 with nivolumab and chemotherapy in pancreatic cancer & potential serum biomarkers. *Cancer Res.* **85**, 7141–7141 (2025).
53. Shi, Y. et al. Decoding the multicellular ecosystem of vena caval tumor thrombus in clear cell renal cell carcinoma by single-cell RNA sequencing. *Genome Biol.* **23**, 87 (2022).
54. Gao, R. et al. Delineating copy number and clonal substructure in human tumors from single-cell transcriptomes. *Nat. Biotechnol.* **39**, 599–608 (2021).
55. Stuart, T. et al. Comprehensive integration of single-cell data. *Cell* **177**, 1888–1902 e1821 (2019).
56. Finak, G. et al. MAST: a flexible statistical framework for assessing transcriptional changes and characterizing heterogeneity in single-cell RNA sequencing data. *Genome Biol.* **16**, 278 (2015).
57. Zhang, Q. et al. Landscape and dynamics of single immune cells in hepatocellular carcinoma. *Cell* **179**, 829–845 e820 (2019).
58. Liberzon, A. et al. The Molecular Signatures Database (MSigDB) hallmark gene set collection. *Cell Syst.* **1**, 417–425 (2015).
59. Ogata, H. et al. KEGG: Kyoto Encyclopedia of Genes and Genomes. *Nucleic Acids Res.* **27**, 29–34 (1999).
60. Jassal, B. et al. The Reactome Pathway Knowledgebase. *Nucleic Acids Res* **48**, D498–D503 (2020).
61. Aleksander, S. A. et al. The Gene Ontology Knowledgebase in 2023. *Genetics* **224**, iyad031 (2023).
62. Sade-Feldman, M. et al. Defining T cell states associated with response to checkpoint immunotherapy in melanoma. *Cell* **176**, 404 (2019).
63. Subramanian, A. et al. Gene set enrichment analysis: a knowledge-based approach for interpreting genome-wide expression profiles. *Proc. Natl. Acad. Sci. USA* **102**, 15545–15550 (2005).
64. Qiu, X. et al. Reversed graph embedding resolves complex single-cell trajectories. *Nat. Methods* **14**, 979–982 (2017).
65. Qiu, X. et al. Single-cell mRNA quantification and differential analysis with Census. *Nat. Methods* **14**, 309–315 (2017).
66. Cao, J. et al. The single-cell transcriptional landscape of mammalian organogenesis. *Nature* **566**, 496–502 (2019).
67. La Manno, G. et al. RNA velocity of single cells. *Nature* **560**, 494–498 (2018).
68. Qiu, X. et al. Mapping transcriptomic vector fields of single cells. *Cell* **185**, 690–711 e645 (2022).
69. Jin, S. et al. Inference and analysis of cell-cell communication using CellChat. *Nat. Commun.* **12**, 1088 (2021).
70. Hu, J. et al. Tumor microenvironment remodeling after neoadjuvant immunotherapy in non-small cell lung cancer revealed by single-cell RNA sequencing. *Genome Med* **15**, 14 (2023).
71. Choudhary, S. & Satija, R. Comparison and evaluation of statistical error models for scRNA-seq. *Genome Biol.* **23**, 27 (2022).
72. Zhou, Z., Zhong, Y., Zhang, Z. & Ren, X. Spatial transcriptomics deconvolution at single-cell resolution using Redeconve. *Nat. Commun.* **14**, 7930 (2023).
73. Zhang, Q. et al. The extracellular-matrix-remodeling capability exposes therapeutic vulnerability in a subset of renal cell carcinomas with tumor thrombi. *Dev. Cell* **60**, 3201–3221 e3215 (2025).
74. Xiong, S. et al. Single-cell and spatial transcriptomic analysis reveal cellular heterogeneity and cancer cell-intrinsic major histocompatibility complex II expression in urothelial carcinoma. *Int J. Biol. Sci.* **21**, 6649–6673 (2025).
75. Yang, J. et al. Spotiphy enables single-cell spatial whole transcriptomics across an entire section. *Nat. Methods* **22**, 724–736 (2025).
76. McDermott, D. F. et al. Clinical activity and molecular correlates of response to atezolizumab alone or in combination with bevacizumab versus sunitinib in renal cell carcinoma. *Nat. Med.* **24**, 749–757 (2018).
77. Motzer, R. J. et al. Avelumab plus axitinib versus sunitinib for advanced renal-cell carcinoma. *N. Engl. J. Med.* **380**, 1103–1115 (2019).
78. Braun, D. A. et al. Interplay of somatic alterations and immune infiltration modulates response to PD-1 blockade in advanced clear cell renal cell carcinoma. *Nat. Med* **26**, 909–918 (2020).
79. Zhang, H. et al. Proteogenomics of clear cell renal cell carcinoma response to tyrosine kinase inhibitor. *Nat. Commun.* **14**, 4274 (2023).
80. Mariathasan, S. et al. TGFbeta attenuates tumour response to PD-L1 blockade by contributing to exclusion of T cells. *Nature* **554**, 544–548 (2018).
81. Liu, D. et al. Integrative molecular and clinical modeling of clinical outcomes to PD1 blockade in patients with metastatic melanoma. *Nat. Med* **25**, 1916–1927 (2019).
82. Zhang, J. et al. Single-cell analysis reveals that vitamin c inhibits bone metastasis of renal cancer via cell cycle arrest and microenvironment remodeling. *Adv. Sci.* **12**, e01011 (2025).

83. Cancer Genome Atlas Research, N. Comprehensive molecular characterization of clear cell renal cell carcinoma. *Nature* **499**, 43–49 (2013).
84. Guo, X. et al. Contrasting cytotoxic and regulatory T cell responses underlying distinct clinical outcomes to anti-PD-1 plus lenvatinib therapy in cancer. *Cancer Cell* **43**, 248–268 e249 (2025).
85. Ghosh, S. et al. Impact of sunitinib resistance on clear cell renal cell carcinoma therapeutic sensitivity in vitro. *Cell Cycle* **23**, 43–55 (2024).
86. Liu, Z. et al. A single-cell atlas reveals immune heterogeneity in anti-PD-1-treated non-small cell lung cancer. *Cell* **188**, 3081–3096 e3019 (2025).
87. Chen, Y. et al. Spatiotemporal single-cell analysis decodes cellular dynamics underlying different responses to immunotherapy in colorectal cancer. *Cancer Cell* **42**, 1268–1285 e1267 (2024).

Acknowledgements

The authors thank the patients who participated in this study and their families. We are grateful to the clinical staff and data managers at PLAGH for their support in patient care and sample collection. We also sincerely thank Professor Weiqiang Jing from Qilu Hospital of Shandong University for his valuable guidance on in vitro neutrophil experiments. In addition, we acknowledge the research teams who made their datasets publicly available and thereby enabled cross-cohort validation in this study. This work was supported by the National Natural Science Foundation of China (82372704, B.W.; 82373169 and 82573476, L.G.; 82341030 and 82173061, W.C.), the Beijing Natural Science Foundation (L248017, Q.H.), the PLA General Hospital Cultivation Program for the National Science Fund for Distinguished Young Scholars (no. 202002, B.W.) and and the PLA General Hospital Intramural Research Program (2024BJ-05, L.G.). We thank ChatGPT (OpenAI) for assistance in refining portions of the manuscript, Editage (www.editage.cn) for English language editing and Figdraw for figure preparation (Figs. 4c and 6a; www.figdraw.com; license ID: WSRAR544a7).

Author contributions

L.G., Q.Z., Q.L., C.P., X.L., X.Z., X.M., W.C., and B.W. conceived and designed the study. L.G., Q.Z., Q.L., W.C., and B.W. developed the methodology. Q.L., Y.Z., Q.B. and Y.W. performed experimental validation. L.G., Q.Z., Q.L., C.P., C.W., J.L., Q.H., Z.L., and Y.H. carried out investigation and data collection. Q.Z., Q.L., L.G., C.P., C.W., and Y.H. curated and organized the data. Q.Z. and Y.T. performed bioinformatics analysis and data visualization. L.G., Q.Z., C.P., and Q.L. drafted the manuscript. L.G., Q.Z., Q.L., C.P., X.Z., B.W., X.M., and W.C. reviewed and edited the manuscript. X.Z., L.G., X.M., W.C., and B.W. acquired funding and provided study resources. X.Z., X.M., W.C., and B.W. supervised the study. All authors reviewed and approved the final manuscript.

Competing interests

The authors declare no competing interests.

Additional information

Supplementary information The online version contains supplementary material available at https://doi.org/10.1038/s41467-026-70978-z.

Correspondence and requests for materials should be addressed to Yan Huang, Xu Zhang, Xin Ma, Weimin Ci or Baojun Wang.

Peer review information *Nature Communications* thanks Zhiliang Bai, Yi-Zhou Jiang, Yi Dong and the other anonymous reviewer for their contribution to the peer review of this work. A peer review file is available.